"3D_Fault_Offsets," a Matlab Code to Automatically Measure Lateral and Vertical Fault Offsets in Topographic Data: Application to San Andreas, Owens Valley, and Hope Faults

N. Stewart, Y. Gaudemer, I. Manighetti, L. Serreau, A. Vincendeau, Stephane Dominguez, L. Matteo, Jacques Malavieille

AGU PUBLICATIONS

JGR

Journal of Geophysical Research: Solid Earth

RESEARCH ARTICLE
10.1002/2017JB014863

Key Points:
- We developed a Matlab code to automate lateral and vertical fault offset measurements and their uncertainties in topographic data
- We remeasured offsets across 88 markers on San Andreas, Owens Valley, and Hope faults. The new and prior offsets compare well
- We performed 5,454 lateral and vertical offset measures. The rich record provides new insights on preservation of fault offsets in morphology

Supporting Information:
- Supporting Information S1
- Data Set S1
- Data Set S2
- Data Set S3
- Data Set S4
- Data Set S5
- Data Set S6
- Table S1
- Table S2
- Table S3
- Table S4

Correspondence to:
I. Manighetti,
manighetti@geoazur.unice.fr

Citation:
Stewart, N., Gaudemer, Y., Manighetti, I., Serreau, L., Vincendeau, A., Dominguez, S., … Malavieille, J. (2018). "3D_Fault_Offsets," a Matlab code to automatically measure lateral and vertical fault offsets in topographic data: Application to San Andreas, Owens Valley, and Hope faults. *Journal of Geophysical Research: Solid Earth*, *123*, 815–835. https://doi.org/10.1002/2017JB014863

Received 13 AUG 2017
Accepted 21 DEC 2017
Accepted article online 28 DEC 2017
Published online 15 JAN 2018

"3D_Fault_Offsets," a Matlab Code to Automatically Measure Lateral and Vertical Fault Offsets in Topographic Data: Application to San Andreas, Owens Valley, and Hope Faults

N. Stewart[1], Y. Gaudemer[2], I. Manighetti[1], L. Serreau[1], A. Vincendeau[1], S. Dominguez[3], L. Mattéo[1], and J. Malavieille[3]

[1]Université Côte d'Azur, OCA, IRD, CNRS, Géoazur, Valbonne Sophia Antipolis, France, [2]Institut de Physique du Globe de Paris, Sorbonne Paris Cité, Université Paris Diderot, CNRS, Paris, France, [3]Géosciences Montpellier, CNRS, Montpellier, France

Abstract Measuring fault offsets preserved at the ground surface is of primary importance to recover earthquake and long-term slip distributions and understand fault mechanics. The recent explosion of high-resolution topographic data, such as Lidar and photogrammetric digital elevation models, offers an unprecedented opportunity to measure dense collections of fault offsets. We have developed a new Matlab code, 3D_Fault_Offsets, to automate these measurements. In topographic data, 3D_Fault_Offsets mathematically identifies and represents nine of the most prominent geometric characteristics of common sublinear markers along faults (especially strike slip) in 3-D, such as the streambed (minimum elevation), top, free face and base of channel banks or scarps (minimum Laplacian, maximum gradient, and maximum Laplacian), and ridges (maximum elevation). By calculating best fit lines through the nine point clouds on either side of the fault, the code computes the lateral and vertical offsets between the piercing points of these lines onto the fault plane, providing nine lateral and nine vertical offset measures per marker. Through a Monte Carlo approach, the code calculates the total uncertainty on each offset. It then provides tools to statistically analyze the dense collection of measures and to reconstruct the prefaulted marker geometry in the horizontal and vertical planes. We applied 3D_Fault_Offsets to remeasure previously published offsets across 88 markers on the San Andreas, Owens Valley, and Hope faults. We obtained 5,454 lateral and vertical offset measures. These automatic measures compare well to prior ones, field and remote, while their rich record provides new insights on the preservation of fault displacements in the morphology.

1. Introduction

Knowing how much slip a fault has accumulated during one earthquake or over the long-term is important in many aspects including a better understanding of fault kinematics and mechanics (e.g., Armijo et al., 1989; Gaudemer et al., 1989, 1995; Hubert-Ferrari et al., 2002; Manighetti et al., 2001; Manighetti, King, & Sammis, 2004; Replumaz et al., 2001; Van der Woerd et al., 1998, 2002), relations between earthquake and cumulative slips (e.g., Gaudemer et al., 1989; Li et al., 2012; Manighetti et al., 2005; Peltzer et al., 1988; Tapponnier et al., 2001; Zielke, Klinger, & Arrowsmith, 2015), and earthquake magnitude and stress distribution (e.g., Klinger et al., 2011; Lasserre et al., 1999; Manighetti, Caulet, et al., 2015; Perrin et al., 2016; Zielke et al., 2012). Yet while current earthquake slip can generally be measured or estimated both along-strike and along-dip of the ruptured fault (e.g., Manighetti et al., 2005; Yeats et al., 1997), long-term cumulative slip can generally only be measured along the fault strike at the ground surface. Surface slip measurements are thus of critical importance to recover how cumulative displacements, including prehistorical earthquake slips, are distributed along faults.

Fault slips at the surface are generally preserved in the form of fault-offset sublinear geomorphic markers (e.g., Arrowsmith & Zielke, 2009; Burbank & Anderson, 2011; Knuepfer, 1987; McCalpin, 2009; Sieh, 1984; Wallace, 1968, 1990, Figure 1). These markers are commonly persistent or ephemeral stream channels (Lensen, 1968; Lienkaemper, 2001; McCalpin, 2009; Sieh, 1978; Wallace, 1968, 1990; Zielke et al., 2010; Figure 1) or abandoned alluvial terrace risers (e.g., Gold et al., 2009, 2011; Lensen, 1964, 1968; Pazzaglia, 2013; Van der Woerd et al., 2002). The creation and preservation of these offset markers require an equilibrium between tectonic (fault slip, warping, and tilting), alluvial (sedimentation and erosion), and

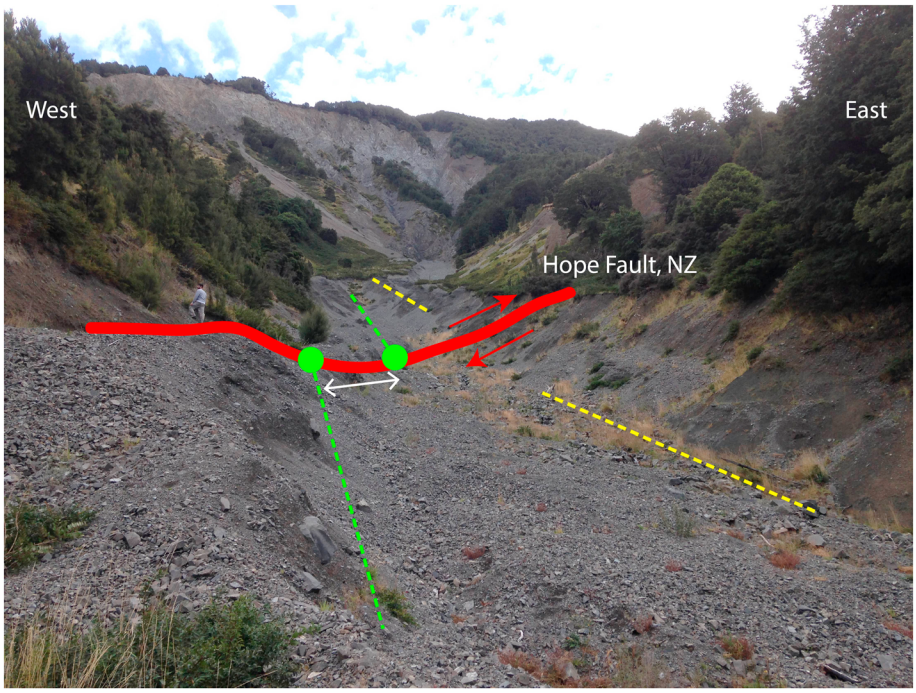

Figure 1. Field view of a dextrally offset channel, Hope fault, New Zealand (picture is courtesy of J. Malavieille). The channel is the 16/17-no marker originally measured by Manighetti, Perrin et al. (2015) and that was measured here (see Table ES-D).

geomorphic (erosion) processes and rates (Bull, 1991; Burbank & Anderson, 2011; Lienkaemper, 2001; Ludwig et al., 2010; McCalpin, 2009; Ouchi, 2005; Salisbury et al., 2012; Sieh, 1978; Wallace, 1968; Zielke et al., 2012, 2015). These conditions pose a number of challenges (e.g., Gold et al., 2009, 2011; McCalpin, 2009; Ouchi, 2005; Salisbury et al., 2012; Scharer et al., 2014; Zielke et al., 2015): how to evaluate the degree of preservation (or erosion) of an offset marker, that is, its accuracy to represent the actual fault slip? How to measure the three components of the fault displacement across an offset marker? How to perform such complex measurements in an efficient way on a dense population of offset markers?

Until recently, offset markers have been measured "manually," especially along strike-slip faults (e.g., Ansberque et al., 2016; Armijo et al., 1989; Frankel et al., 2007; Gaudemer et al., 1989; Gold et al., 2009; Hubert-Ferrari et al., 2002; Klinger et al., 2011; Li et al., 2012; Replumaz et al., 2001; Ritz et al., 1995; Rizza et al., 2015; Sieh, 1978; Van der Woerd et al., 1998, 2002). A fault-offset marker is identified visually by the expert in satellite, aerial images, or on the field (Figure 1). Then the expert manually performs a retrodeformation, or back slip, which is the stepwise reconstruction of 2-D horizontal views (more rarely vertical sections) to realign the likely original map-view trace of the marker (e.g., McCalpin, 2009). The preferred reconstruction provides the horizontal offset value along the fault strike or, more rarely, the vertical value along the fault dip. This classical method has shown to be relevant in the many studies that have used it for decades (references above). However, offset measures and their uncertainties are derived solely from visual interpretations that might thus be disputed. Only the horizontal component of the slip is generally estimated. Also, the reconstruction of the marker provides only a map view vision of its original morphology, and the measurement is time consuming.

More recently, the explosion of high-resolution topographic data, especially Lidar that allows the measurement of the bare Earth surface at $\leq$1 m resolution (e.g., Arrowsmith & Zielke, 2009; Bevis et al., 2005; De Pascale et al., 2014; Frankel et al., 2007; Haddad et al., 2012; Lin et al., 2013; Meigs, 2013; Zielke et al., 2012; Zielke et al., 2015), has motivated the development of new, automatized approaches to remotely measure fault slips in the topographic data. These approaches, so far, use an overall measure of the topography (Billant et al., 2016), planar surfaces (Mackenzie & Elliott, 2017), or linear geomorphic features (Haddon et al., 2016; Zielke et al., 2012; Zielke & Arrowsmith, 2012) as recorders and markers of the fault displacements. In particular, Zielke and Arrowsmith (2012) and Zielke et al. (2012) have developed a Matlab code, LaDiCaoz (updated version, LaDiCaoz_v2, released by Haddon et al., 2016), to semiautomatically measure fault offsets

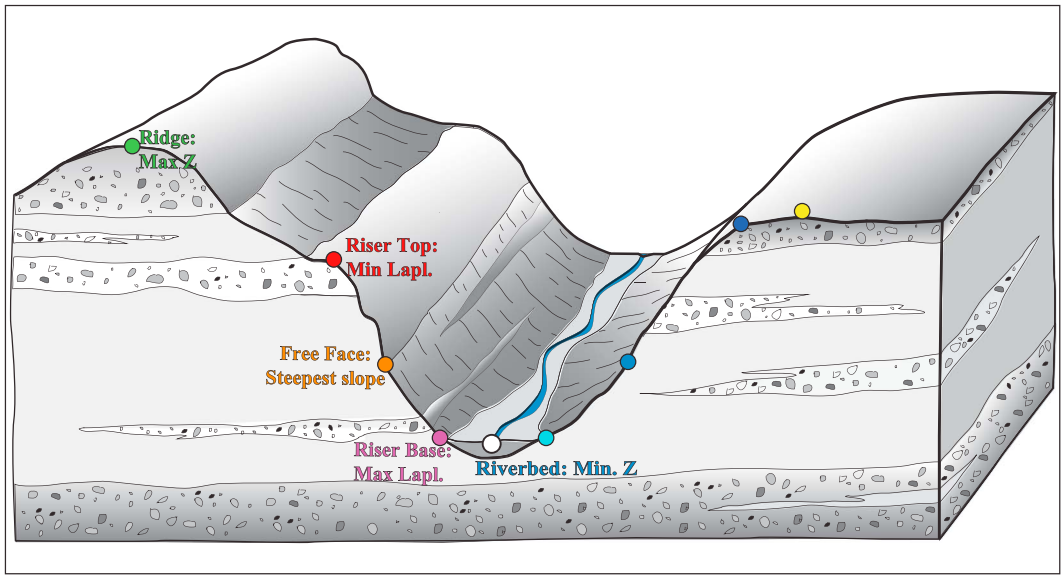

Figure 2. Idealized representation of the nine geometric features identified mathematically by the 3D_Fault_Offsets code.

across ubiquitous linear geomorphic features such as stream channels and terrace risers. LaDiCaoz correlates two along-fault profiles crossing an offset marker on either side of the fault trace. The best fit correlation provides a measure of the lateral and the vertical offsets of the marker. Errors are estimated from the range of back slip reconstructions that the user estimates as being plausible. This automatized method has proven to be relevant and efficient in the many studies that have used it (Haddon et al., 2016; Ren et al., 2016; Salisbury et al., 2012; Zielke et al., 2010, 2012). Its efficiency was especially clear in that it allowed measuring hundreds of offsets along a fault, about 10 times more than ever before. However, LaDiCaoz includes a number of user interactions and primarily analyzes offset markers in 2-D.

Here we have developed a new Matlab code, 3D_Fault_Offsets, which, in topographic data, mathematically identifies and represents in 3-D the most prominent geometric characteristics of ubiquitous geomorphic sublinear markers along faults. Faults can have any dip, but the code is especially appropriate for strike-slip faults. Nine geometric characteristics are identified across each offset marker section on either side of a fault (Figure 2 described below), which are then converted into nine individual horizontal and vertical displacement measurements across each marker. The code also calculates the total 3-D uncertainties on these offsets. Finally, it provides tools to statistically analyze the collection of measurements, and to reconstruct the likely original marker geometry in both the horizontal and the vertical planes.

To test the robustness of 3D_Fault_Offsets, we have applied it to remeasure the offsets across 88 markers that were analyzed in prior works (Haddon et al., 2016; Lienkaemper, 2001; Manighetti, Perrin, et al., 2015; Sieh, 1978; Zielke et al., 2012). We assume that these previous studies have correctly identified the markers and their respective offsets. The markers extend along three faults, San Andreas and Owens Valley in USA and Hope in New Zealand, that have different slip modes (purely strike slip, strike slip and normal, and strike slip and reverse, respectively) and morphological environments (from moderate to significant erosion conditions). The topographic data that we use have different resolutions (0.25 cm to 1 m). In total, we have performed 303 series of measures (i.e., code runs, each including 9 lateral and 9 vertical offset measures), representing a total of 5,454 lateral and vertical offset measures, and compared these offset measures to previously published field and remote measurements.

2. Overview of 3D_Fault_Offsets

Note that 3D_Fault_Offsets is described in greater detail in supporting information ES1 and provided as a zip file in the supporting information named 3D_FAULT_OFFSETS_CODE.zip.

3D_Fault_Offsets is designed to process high-resolution topographic data such as Lidar, but it can be used with any type of topographic data storing surface elevation information on a rasterized grid (digital

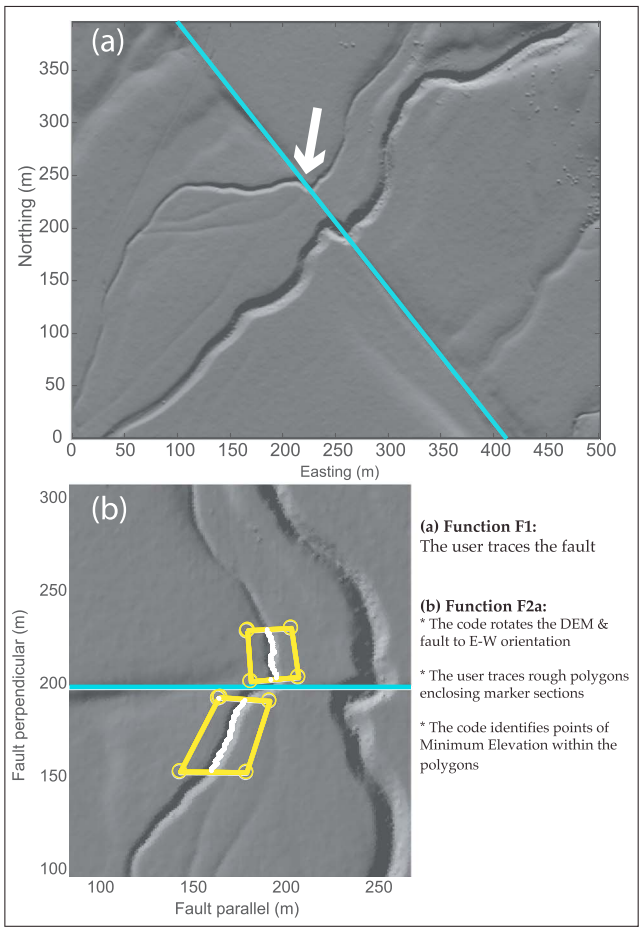

Figure 3. (a) Hillshade representation of a DEM region (here at 1 m resolution) including two offset channels (southern San Andreas Lidar data; Zielke et al., 2012) and fault trace (blue) drawn by the user. The white arrow indicates the ZA6808a marker that is illustrated in following figures. (b) Once the user has traced the fault, the code rotates the DEM and fault to an E-W attitude. When the user has traced the two polygons around the marker sections of interest, the code identifies the points of minimum elevation within the polygons and populates the DEM with those points (white). They underline the riverbed. In this figure and following (Figures 3–6 and additional ones in supporting information ES1), the example has been processed using 1 m resolution Lidar data to enhance the clarity of the figures.

elevation model or DEM). The code is dedicated to analyze sublinear geomorphic markers, which are those most commonly used for fault offset analysis (e.g., McCalpin, 2009; Salisbury et al., 2015; Scharer et al., 2014). To operate 3D_Fault_Offsets, the user must first identify the fault trace and the two marker sections offset by the fault. The tectonic relevance of the fault and marker identification is assessed by the user. The markers must be analyzed on a case-by-case basis, which, in effect, limits the size of the fault zone under analysis. 3D_Fault_Offsets can incorporate any fault dip, and the user is invited to provide this information.

3D_Fault_Offsets functions as scripts written in Matlab. It includes 15 related functions F1 to F7bis and 1 additional routine (F8) made to supplement the analysis. We provide the code as a single wrap-around Matlab file (F0) containing interactive questions and operating instructions that lead the user to easily run the different functions consecutively. Alternatively, the user can choose to use each function individually. The operation of these files requires only very basic knowledge of Matlab procedures. To operate 3D_FAULT_OFFSETS, the user needs to have the matGeom toolbox (it can be freely downloaded from its repository on the Matlab website).

Within a polygon zone defined by the user that roughly includes a marker section on one side of a fault (fault trace drawn by the user; Functions F1 and F2) (Figures 3a and 3b), 3D_Fault_Offsets mathematically identifies the topographic data points that characterize nine prominent geometric features prevalent in most geomorphic markers (Figure 2): riverbed, identified as the zone of lowest elevation (Min Z referred to as "river," one point cloud); riser or scarp base and top (referred to as "bot" and "top"), identified through

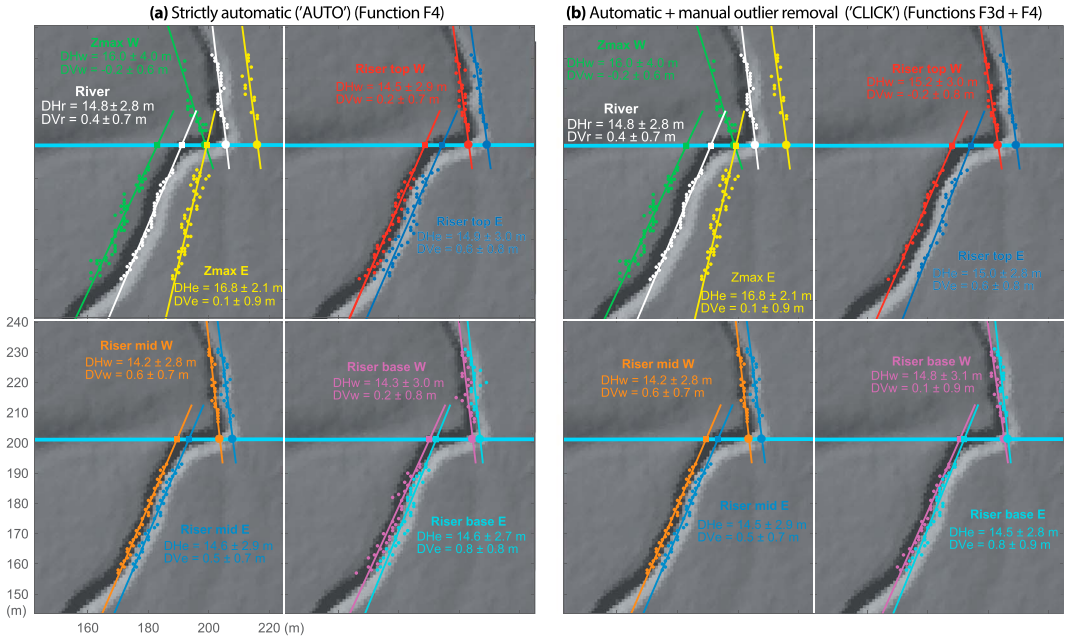

Figure 4. (a) Using the "cleaned" best fit lines, the code calculates the lateral and vertical offsets by subtracting the *x* and *z* coordinates of the piercing points of their respective best fit lines on either side of the fault. Uncertainties on the offsets are also calculated. The calculations are here strictly automatic (AUTO approach). (b) Similar offset calculations but performed after the user have manually removed a few outlier points in the point clouds (CLICK approach).

their slope break using the maximum (i.e., maximum convexity of slope) and minimum Laplacian (i.e., maximum concavity of slope) of the topography, respectively (four point clouds on either side of a riverbed); riser or scarp steepest central part or "free face" (referred to as "mid"), identified through the measurement of the maximum gradient of the topography (two point clouds on either side of a riverbed); and the ridge or crest identified as the zone of maximum elevation (referred to as "Max Z"; two point clouds on either side of a riverbed). For every marker, the code searches for the nine specific features systematically along fault parallel topographic profiles that cover the entirety of the polygon zone (two series of profiles on either side of the riverbed, see supporting information ES1). This eventually populates the polygon zone with a great density of points, forming nine individual point clouds.

Using the least squares method, the code then computes a 3-D linear regression through each of the nine point clouds on either side of the fault, in effect creating 18 lines of best fit (Function F3, Figure ES1_B(a) in supporting information ES1). After this first regression, the code removes the artifact points related to the polygon edges and the obvious outliers of the lines through the implementation of the interquartile method (Function F3b, Figure ES1_B(b) in supporting information ES1). It then recalculates the best fit lines from these "cleaned" point clouds (Function F3b, Figure ES1_B(b) in supporting information ES1). The eventual best fit lines characterize the marker geometry in 3-D. The F3e function informs the user of the number of points used in each best fit line calculation, allowing for the verification of its statistical relevance. Each 3-D line of best fit intersects the dipping fault plane creating a piercing point whose *x*, *y*, and *z* coordinates are recorded. The underlying hypothesis is that, as commonly assumed (e.g., McCalpin, 2009), paired piercing points (i.e., characterizing the same geometric feature) on either side of the fault were initially the same "prefaulted" point.

Based upon that assumption, the code computes the three components of the slip vector that joins the paired piercing points. It specifically calculates the horizontal and vertical offsets by subtracting the *x* and *z* coordinates of the corresponding piercing points on either side of the fault (Figure 4a; Function F4; if needed, the *y* component can be derived from the other two slip components). The 18 offset calculations are done systematically regardless of their geomorphic relevance, which can be defined subsequently.

The uncertainties are computed (Function F4) from the various sources of error, which include the resolution of the DEM, the position of each point contributing to a best fit line, the position of the piercing points onto the fault plane, and the errors on the fault position, strike, and dip. The DEM resolution is one of the largest

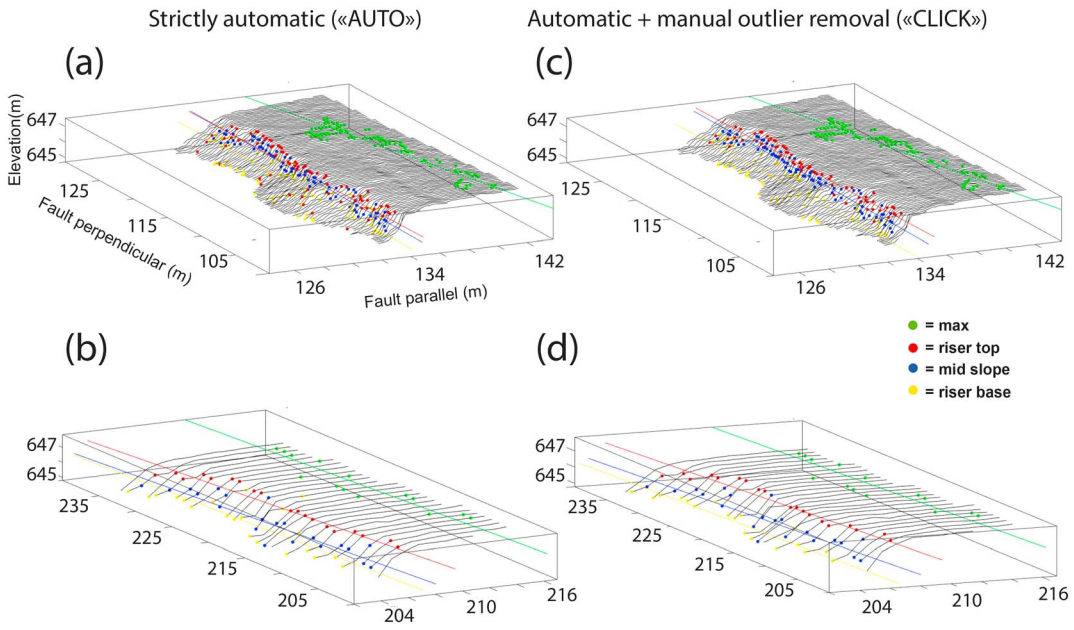

Figure 5. (a–d) 3-D rotated views of the NE side of the marker ZA6808a shown in Figures 3 and 4. The distribution of the identified points and corresponding best fit lines can be seen onto the DEMs and compared between the two DEM resolutions (25 cm and 1 m). The views show that the "click" calculations we did in the 25 cm data (Figure 5c) could have been more optimal (a few outlier points obviously remain to be removed). The corresponding measurements are in Tables ES-A and ES-B.

sources of error due to its effect on the positioning of the individual points defining the respective feature. To deal with these multiple sources of error, the code utilizes a Monte Carlo approach that is described in supporting information ES1.

The code is entirely automatic, yet it offers the possibility to manually remove outlier points before calculating the offsets (Function F3d, Figures 4b and ES1_D in supporting information ES1). Function F3c allows the user to visualize the distribution of the points and best fit lines on the DEM in rotating 3-D views (Figures 5 and ES1_C in supporting information ES1). This is helpful both to identify the possible outlier points and to judge the geomorphic relevance of the calculated regressions.

The nine lateral and the nine vertical offset measures provide a unique opportunity to examine the variability of the offsets across the entirety of the marker. As commonly performed (e.g., Beauprêtre et al., 2012, 2013; Lowell, 1995; Manighetti, Perrin, et al., 2015; McGill & Sieh, 1991; Scharer et al., 2014; Zechar & Frankel, 2009; Zielke et al., 2012), the code uses probability density functions (PDFs) to derive the most robust offset values and their uncertainties (Figure ES1_F in supporting information ES1). The "best offsets" are estimated by calculating the best fitting Gaussian of the summed PDF function, with their uncertainties being the 1 sigma width of the Gaussian (Figure ES1_F in supporting information ES1). These "best-Gaussian" uncertainties represent the largest possible errors on the offsets for they integrate the full range of offset variability (Figure ES1_F in supporting information ES1). Commonly, a more realistic uncertainty can be derived from the zone of highest and most concentrated peaks in the summed PDF function (Figure ES1_F in supporting information ES1). In the following, we provide both maximum and preferred uncertainties.

The code eventually reconstructs the marker both in a horizontal and a vertical plane (Figure 6 and supporting information ES3, ES4, and ES6). These back slip reconstructions allow the user to verify the geomorphic and tectonic relevance of the offset measures.

3. Possible Artifacts and Sensitivity of 3D_Fault_Offsets

3.1. Possible Artifacts

Different sources of artifacts related to the topographic data or to the calculation methods can affect the point identification and hence the offset calculations.

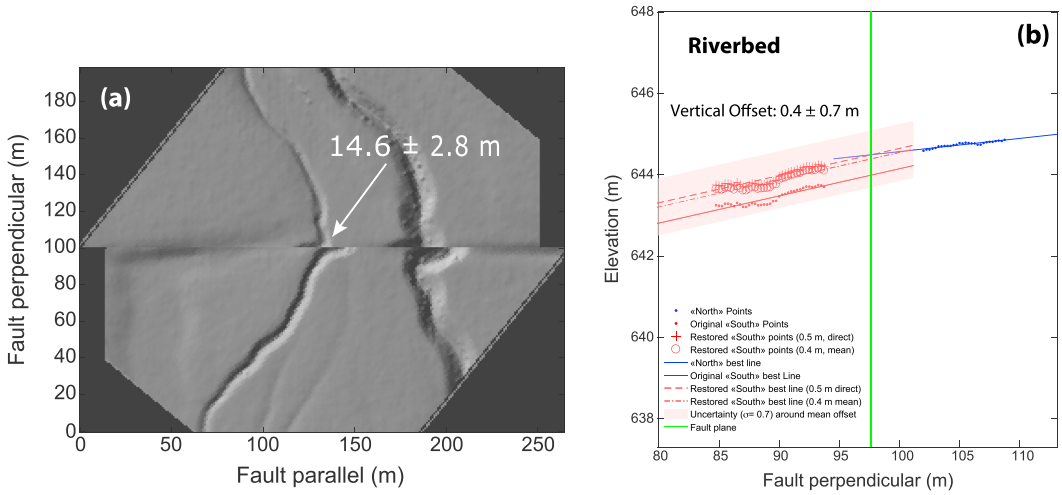

Figure 6. (a) Horizontal back slip of the marker performed by the code, using the offset value provided by the user (here, optimal lateral offset). (b) Vertical back slip of the riverbed of the marker. The back slip is performed using the "direct" vertical offset (see details in supporting information ES1), but the mean vertical offset is shown along with its uncertainty. Here the vertical offset is about null, what explains the large relative uncertainties. Data are in Table ES-B.

The polygon edges are physical point clouds that disrupt the calculations at the zone edges and produce artifact points. Since these artifact points are systematic, we have included Function F3b to automatically remove them before calculating the final best fit lines (supporting information ES1).

In a similar manner, points at the "internal" tips (i.e., adjacent to riverbed) of the topographic profiles used for calculations may alter some of these calculations. In particular, the Laplacian involves a linear extrapolation of points outside of the domain under analysis, which may produce artifact points misleadingly placed at the tip of the profiles (Figure 5a, ES1_C in supporting information ES1, and ES2_A-B-C in supporting information ES2). Since these artifacts are not systematic, however, we have opted for their manual removal if necessary (Function F3d).

Lidar data, as any other geophysical imaging data, inherently include corduroy artifacts, mainly as a result of the vertical misalignment of the multiple scan lines (e.g., Arrowsmith & Zielke, 2009). The corduroy produces fairly regular troughs and ridges perpendicular to the flight direction with meter-scale wavelengths and decimeter amplitudes, and the effects of these artifacts should be considered when processing the topographic data prior to their use with 3D_Fault_Offsets. In the Lidar data we use here, the corduroy effect was minimized in their prior processing (Arrowsmith & Zielke, 2009; Haddon et al., 2016; Manighetti, Perrin, et al., 2015; Zielke et al., 2012) so that, in the general case, the corduroy height is insignificant compared to the height of the markers' topographic imprint, and therefore, the corduroy artifact does not alter the measurements (Figures 5 and ES1_C in supporting information ES1 and Figure ES2_A in supporting information ES2). More details can be found in supporting information ES1 and ES2.

Some topographic points may display the respective mathematical properties searched by the code while not pertaining to the geometric feature under concern. Those can be points on a neighboring marker, on top of vegetation, on road traces, or simply noise in the data (see example in Figure ES2_D in supporting information ES2). The 3-D views (Function F3c) allow for identifying these artifact points that can then be removed manually.

Overall, the 3-D treatment of topography enables the dense point clouds to generally smooth out these artifacts and reveal the geometric features under concern.

3.2. Sensitivity of the Code

We have verified that when the code is used in constant conditions (same DEM, same fault and polygon traces), the repeatability of the measurements is consistent.

We have conducted a series of tests to assess the sensitivity of the calculations to the polygon width, length, shape, and orientation. Those tests are described in detail in supporting information ES2.

Basically, the code results are not sensitive to the polygon width provided that the polygon region does not include a significant density of diverting features near the marker under concern. As the following data analysis will better show, the offset results are more sensitive to the polygon length because the geometry of the marker traces commonly varies along their length. This is especially the case when the markers are meandering streams or are subjected to erosion. However, regardless of the polygon length, the code produces stable offset values provided that the marker sections enclosed in the polygons encapsulate the overall map-view geometry of the offset marker. Finally, the point identification, best fit line calculations, and lateral and vertical offsets are not affected by the shape and orientation of the polygons.

The DEM resolution is the most impactful parameter affecting the offset results because the placement of the points and thus the calculation of the best fit lines depends on the density of the elevation points in the polygons. In the following analysis, we compare the results obtained on similar markers using Lidar data at 25 cm and 1 m resolution. We find that, regardless of the DEM resolution, the code's reproducibility is consistent provided that the DEM resolution offers a reasonable point density over a marker, at least 1 point per meter length (more details in the next section).

4. Application of 3D_Fault_Offsets to Measure Lateral and Vertical Offsets on San Andreas Fault

4.1. Data and General Approach

We apply 3D_Fault_Offsets to 45 markers (44 stream channels and 1 topographic scarp) along the San Andreas strike-slip fault that were identified in prior works (Lienkaemper, 2001; Sieh, 1978; Zielke et al., 2012). Their lateral offsets were measured both on the field (for 32 of them, Sieh (1978) and Lienkaemper (2001)) and remotely (all 45 markers) using the LaDiCaoz code (Zielke & Arrowsmith, 2012). They vary between ~1 and ~60 m.

We analyze here the northernmost subset of markers reported in Zielke et al. (2012). We picked a few more markers further south that had especially complex traces (low topographic imprint, weathered trace, significant vegetation cover, and trend markedly oblique to the fault; see supporting information ES3) or long traces. The 45 markers had actually been assigned different "qualities" based on the robustness of their identification (Zielke et al., 2012), and the subset analyzed here provides a statistical significance among these qualities (18 markers of high quality, 11 of moderate quality, and 16 of low quality).

We use the same Lidar data as used by Zielke et al. (2012) (data available on www.opentopography.org through the B4 Lidar Project). Their horizontal and vertical resolution is 25 cm (Arrowsmith & Zielke, 2009). However, we have run 3D_Fault_Offsets with a 1 m horizontal and a 0.5 m vertical pixel size as the error inputs, to obtain conservative uncertainties. For each marker, we traced the fault as Zielke et al. (2012) did and considered a constant 90 ± 10° dip at each marker site. We have adopted conservative errors on the fault position (assigned horizontal and vertical errors of 5 and 0.5 m, respectively). Any regression with less than 10 points was discarded from the calculations.

For each marker, we have performed four series of measurements using the 25 cm Lidar data: (i) We have first drawn polygons made to enclose the same marker sections as analyzed by Zielke et al. (2012). These polygons and related calculations are referred to as "AsZ." (ii) We have then used longer and wider polygons relative to the "AsZ," made to enclose a larger portion of the markers and too be less stringent in precisely following the marker traces. These polygons and related calculations are referred to as "Longer." (iii) For each of the AsZ and Longer options, we have made two calculations, the first one entirely automatic referred to as "AUTO," and the second one including a manual user operation to remove the clearest outlying points referred to as "CLICK." Generally, only the "top" and "bot" point clouds were "cleaned," and only a few outliers were removed in each point cloud.

We have then redone the "Longer" measurements (AUTO and CLICK) using the Lidar data at a 1 m resolution.

The four series of measurements in 25 cm Lidar data are reported in Table ES-A and on the figures for each marker in supporting information ES3; they represent 138 series of measures (a series including nine lateral and nine vertical offset measures). The measurements made using the 1 m Lidar data are reported in Table ES-B; they represent 82 series of measures. Together these series make a total of 2,484 lateral and vertical offset measures. When an AsZ or a Longer series is missing, it is because the code was unable to identify

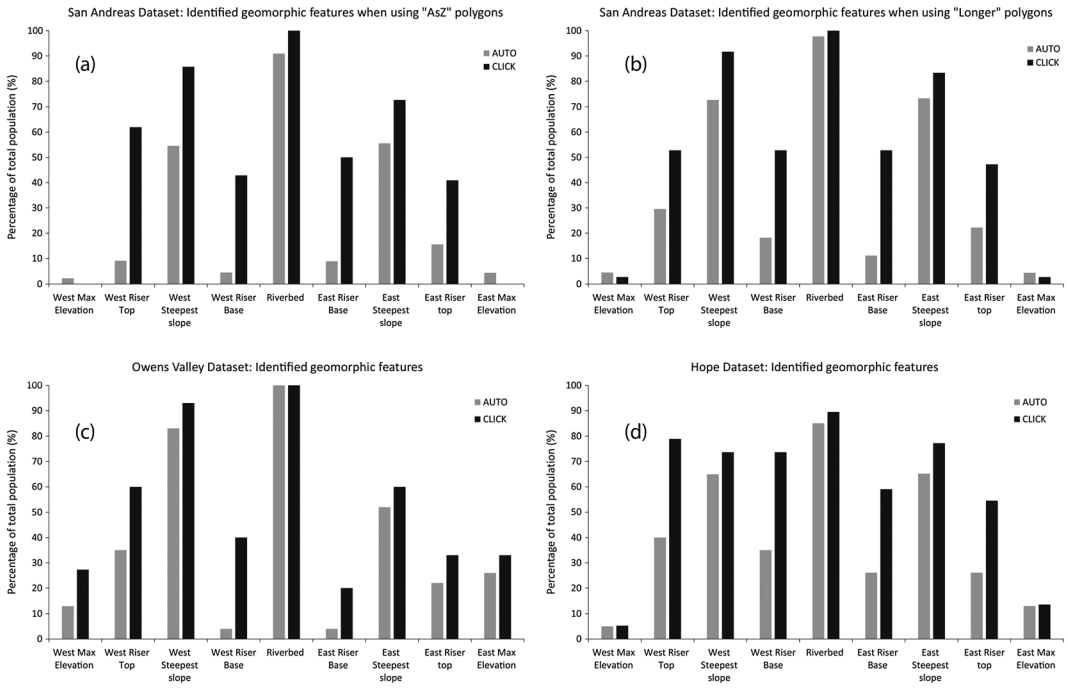

Figure 7. Identified geomorphic features (i.e., with geomorphic relevance) in the three data sets. (a) San Andreas data set (Table ES-A) with measures made using AsZ polygons. (b) San Andreas data set (Table ES-A) with measures made using longer polygons. (c) Owens Valley data set (Table ES-C). (d) Hope data set (Table ES-D). See discussion in text.

the marker, or the marker length was too short to permit any longer polygon. The lack of a CLICK series indicates that no or too few obvious outliers were to be removed.

The 18 best fit line calculations and their visualization in map (supporting information ES3) and rotating 3-D views (examples in Figures 5, ES1_C, and ES2_A to ES2_D) allow for the examination of whether the identified point clouds and the related regressions represent the geomorphic features under concern. At this stage, the user is expected to provide his expertise to decide which regressions and hence which offset measures are geomorphically relevant and should be retained. Reasons for geomorphically irrelevant features include poorly defined regressions, regressions not representing the feature under concern, point clouds containing outliers that could not be removed in any objective manner, etc.; see supporting information ES3). In Table ES-A, we have indicated the offset values that we judge poorly constrained or irrelevant in a geomorphic sense in gray (see table caption) and in black (or red for riverbed) those that we retain as geomorphically meaningful. Later, we refer to "GEOM" as the set of measurements that we consider as geomorphically relevant, and "ALL" as the totality of the measurements with no geomorphic discrimination.

4.2. Overall Analysis of the Offset Measures

In the following, we discuss the automatic measures (AUTO) unless it is said differently. When combining the AsZ and Longer approaches, 3D_Fault_Offsets was able to identify 44 out of the 45 markers (43 stream channels and 1 topographic scarp). The marker that could not be identified is the stream channel Sieh5b, which is very short and has a low topographic imprint.

In all 43 stream channels, the code identifies and properly measures (small rms) the riverbed on either side of the fault, in automatic AsZ and Longer measures (supporting information ES3). Outliers rarely exist in Min Z point clouds, and therefore, the automatic identification of the riverbeds is straightforward.

Beyond the riverbeds, 3D_Fault_Offsets identifies additional geomorphic features in most of the markers. Figure 7 shows the distribution of the identified features that have a geomorphic relevance (values in black in Table ES-A), for the AsZ (Figure 7a) and the Longer approaches (Figure 7b). Overall, considering longer sections of the offset markers allows for better identification and measurement of their geomorphic characteristics. The riverbed is the geomorphic feature most prominently identified in the markers. The riser's

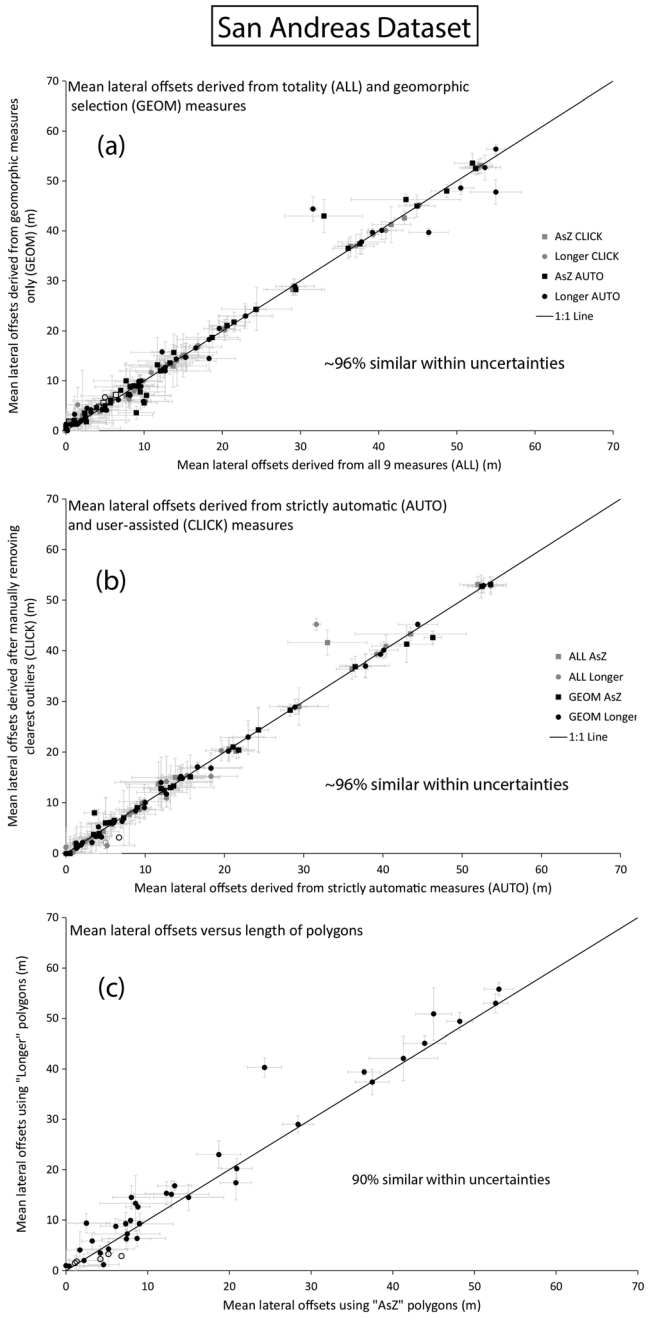

Figure 8. (a) Comparison of the mean lateral offsets measured across the 44 San Andreas markers derived from the totality of the offset measures per marker (column AS in Table ES-A, means noted ALL) and from the geomorphically relevant measures only (column AY in Table ES-A, means noted GEOM). (b) Comparison of the mean lateral offsets measured across the 44 San Andreas markers, with no user action (i.e., strictly automatic approach, "AUTO"), and with a user action that consists of removing the few clearest outlier points from some of the best fit lines, generally the tops and bases ("CLICK") (data in Table ES-A). (c) Comparison of the mean lateral offsets measured across the 44 San Andreas markers, using short (AsZ) and longer (longer) polygons (data in Table ES-A). In all plots, the empty symbols indicate poorly constrained lateral offsets with uncertainties ≥10 m.

steepest slope is the second-most prominent geomorphic feature to be identified well, in ~55% (AsZ) to ~75% (Longer) of the markers. While they are generally not well identified in the AsZ measurements, the riser tops are well-expressed geomorphic features when longer marker sections are considered (identified in ~30% of the cases). The riser bases are more difficult to discriminate, at least in the strictly automatic calculations. It was rare that the point clouds of maximum elevation would highlight any clear geomorphic characteristics of the markers. When the obvious outliers are manually removed ("CLICK" approach, in black in Figure 7), the results are similar but amplified. The major change is that riser bases become better defined.

3D_Fault_Offsets is thus able to identify and mathematically characterize different geomorphic features in a marker. One might argue, however, that the geomorphic relevance of the identified features is not a mathematical output of the code but a subjective ranking by the user. Figure 8a thus examines how the automatic outputs of the code, with no user action, compare with the results derived from user-selected measures. The figure shows the mean lateral offsets derived from the nine measures performed by the code (means noted ALL, Table ES-A), and from the geomorphically relevant measures only (means noted GEOM, Table ES-A). A similar comparison is shown in supporting information ES2 for the vertical offsets (Figure ES2_H(a)). On average, the ALL and GEOM mean lateral offsets are similar within uncertainties in 96% of cases for both the lateral and vertical offsets. Therefore, the offsets derived from the nine systematic and automatic measures of the code are as meaningful as those derived after careful inspection and selection of the geomorphically relevant measures by the expert. This finding should not minimize that the expertise of the user is critical and that the GEOM average offsets are more robustly founded.

Another way to examine the relevance of the automatic approach is to compare the automatic offset measures (AUTO means in Table ES-A) to those derived after manual removal of the clearest outlier points (CLICK means in Table ES-A) (Figure 8b for lateral offsets and Figure ES2_H(b) in supporting information ES2 for vertical offsets). Overall, the measures are consistent, similar within uncertainties in 96% of cases for the lateral offsets, and in 100% of cases for the vertical offsets. Therefore, even though a few outlier points exist in the point clouds mathematically defined by the code, it is not necessary to remove them manually. When average offsets are concerned, the dense automatic measures recover the offset values well.

The above findings suggest that for each series of measures with a given polygon set (AsZ or Longer), the four average offsets derived from (i) the nine automatic measures, strict sense (ALL-A, columns AS and AV in Table ES-A for lateral and vertical, respectively), (ii) the nine automatic measures with manual removal of the few clearest outlier points (ALL-C, columns AS and AV in Table ES-A for lateral and vertical, respectively); (iii) the most geomorphically relevant automatic measures only (GEOM-A, columns AY and BB in Table ES-A for lateral and vertical, respectively), and (iv) the most geomorphically relevant measures with manual removal of the clearest outlier points (GEOM-C, columns AY and BB in Table ES-A for lateral and vertical, respectively) are all consistent. They can thus be combined into a mean global offset, per polygon set (columns BG and BL in Table ES-A for lateral and vertical, respectively). This allows for further

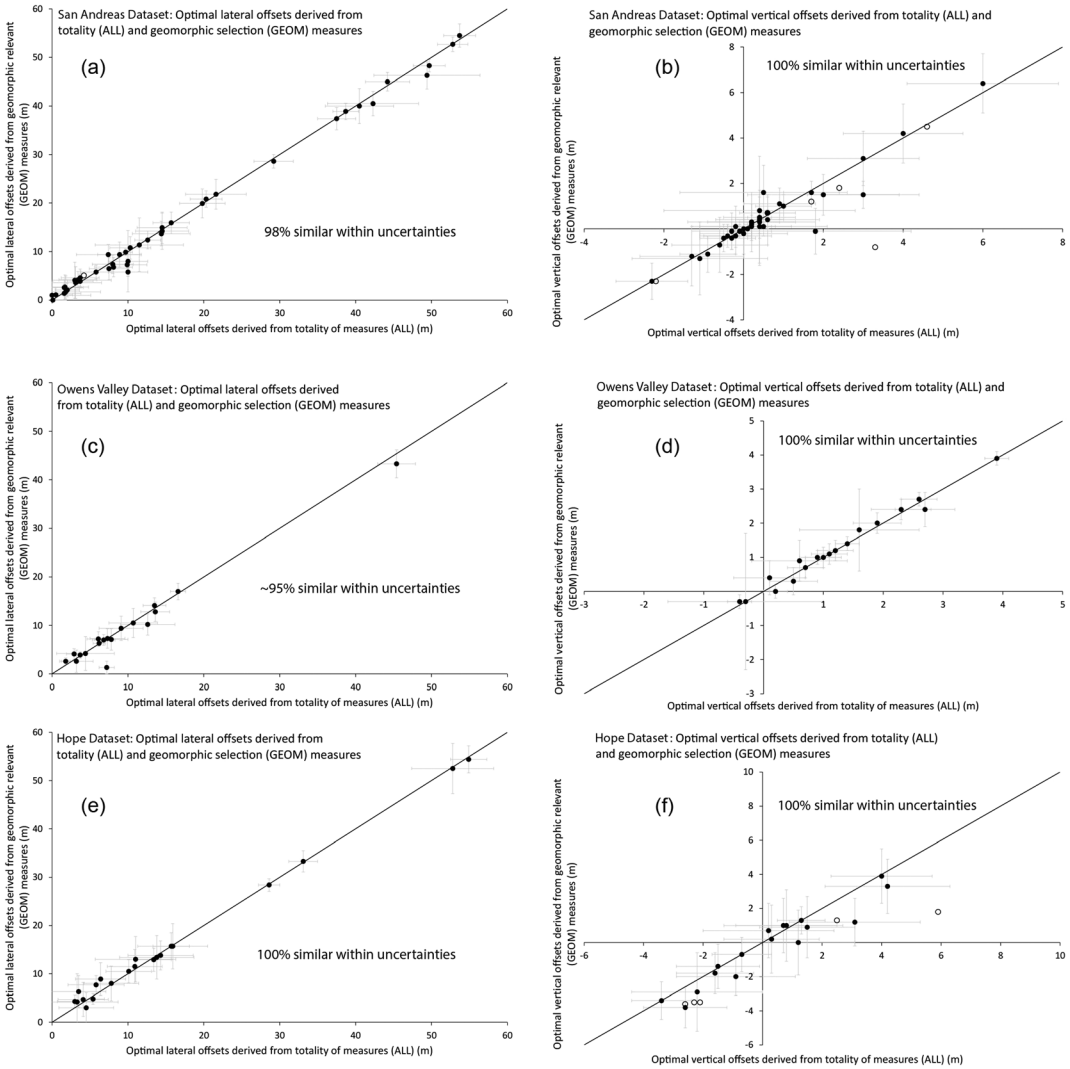

Figure 9. Comparison of the optimal lateral and vertical offsets obtained for the three data sets from the totality of the offset measures per marker (ALL) and from the geomorphically relevant measures only (GEOM) (data in Tables ES-A, ES-C, and ES-D). (a–f) The empty symbols indicate poorly constrained offsets with large uncertainties (≥10 m for lateral and ≥2.5 m for vertical).

examination of the variation of the recovered offsets with the polygon length. Figure 8c compares the mean lateral offsets obtained with AsZ and Longer polygons. Overall, the offsets are consistent and similar within uncertainties for ~90% of cases (similar results for vertical offsets shown in supporting information ES2 (Figure ES2_F)).

Taken together, this analysis suggests that all average offsets discussed above (lateral or vertical) are consistent and equally relevant. We can thus average them to derive a unique global average offset per marker, lateral and vertical, which represents the optimal offset across the marker. Still, we calculate this optimal offset both from the totality of the measures ("ALL," columns BH and BM for lateral and vertical, Table ES-A) and from the geomorphically relevant measures only ("GEOM," columns BI and BN for lateral and vertical, Table ES-A). Figures 9a (lateral) and 9b (vertical) confirm that the two calculations provide similar results, being similar within uncertainties in 98 to 100% of the cases, respectively. We favor the "geomorphic" optimal offsets, however, since they are more robustly founded on the actual marker morphology.

Figure 10 compares our optimal "geomorphic" lateral offsets to prior remote (Figure 10a) and field (Figure 10b) offset measures. The optimal "geomorphic" lateral offsets are similar within uncertainties to prior field and remote measures in ~80% and 90% of cases, respectively. Most differing values are found for low to moderate quality markers. We originally defined the AsZ polygons to represent the marker sections analyzed

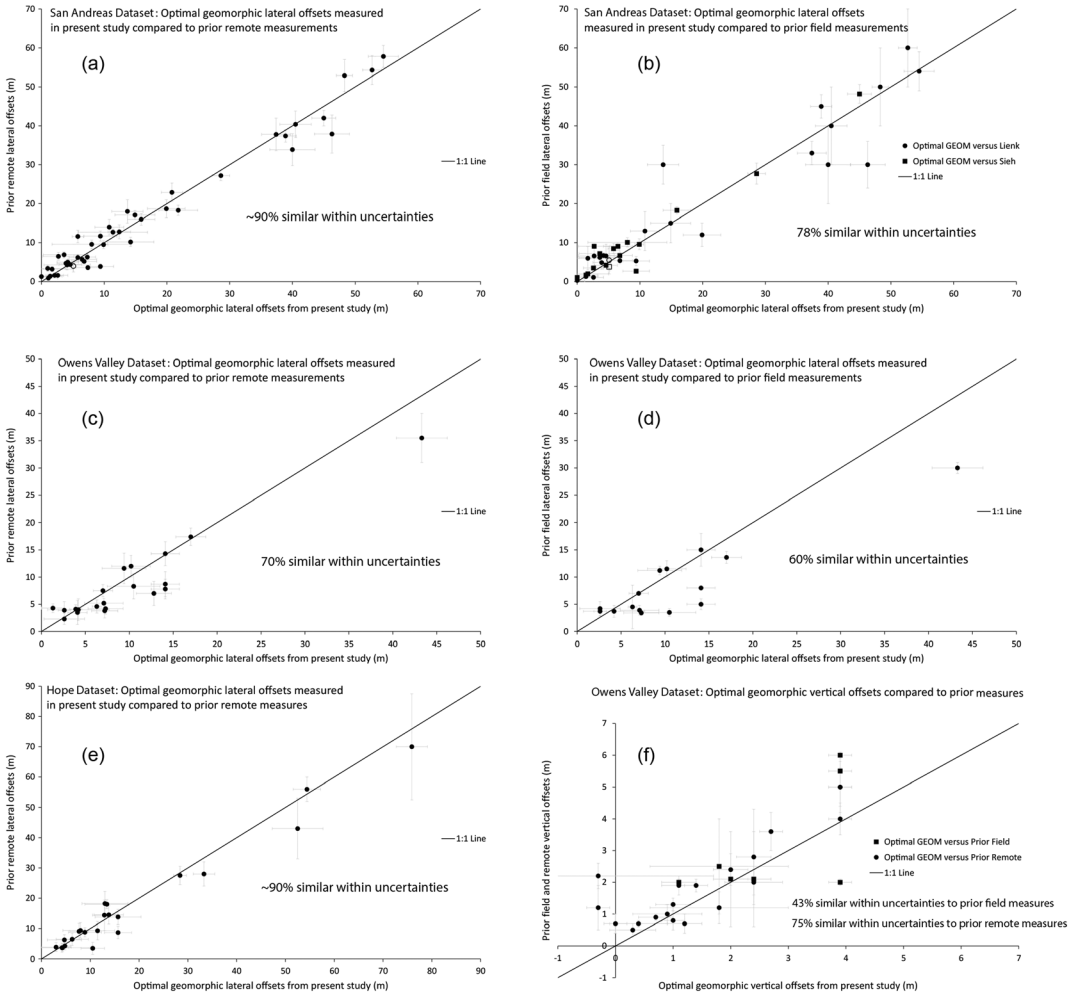

Figure 10. Comparison of geomorphic optimal (GEOM) lateral and vertical offsets obtained in present study with prior field and remote measures. (a) San Andreas data set, lateral offsets compared to prior remote measures. (b) San Andreas data set, lateral offsets compared to prior field measures. (c) Owens Valley data set, lateral offsets compared to prior remote measures. (d) Owens Valley data set, lateral offsets compared to prior field measures. (e) Hope data set, lateral offsets compared to prior remote measures. (f) Owens Valley data set, vertical offsets compared to prior remote measures. The empty symbols indicate poorly constrained lateral offsets with uncertainties ≥10 m.

by Zielke et al. (2012). Figure ES2_I in supporting information ES2 confirms that the mean lateral offsets estimated with AsZ polygons are similar overall to the lateral offsets measured by Zielke et al. (2012) (~90% similar within uncertainties).

While our optimal lateral offsets are similar to prior field and remote estimates, their uncertainties are generally larger than the errors previously suggested (Figure ES2_J(a) in supporting information ES2). The latter are generally proposed to be less than 10–20% of the offset. In our study, approximately 45% of the optimal lateral offsets have an uncertainty lower than 20% of the offset. However, this ratio increases regarding the riverbeds (~60%), showing that riverbeds preserve well the lateral offsets. Conversely, a significant population of the optimal lateral offsets have fairly large errors, greater than the offset in ~15% of the cases. While these larger errors partly result from the conservative approach we have followed, they also likely result from the intrinsic variability among the multiple individual offsets we integrated into the offset calculations.

3D_Fault_Offsets also provides the new opportunity to measure vertical offsets on up to nine geomorphic features (optimal vertical offsets in columns BM (ALL) and BN (GEOM) of Table ES-A). There exists no prior measures against which our optimal vertical offsets can be compared. We note that their uncertainties are large, including for riverbeds (Figure ES2_J(b) in supporting information ES2), mainly because vertical slip is insignificant on the San Andreas Fault (mostly <1 m compromising the limits of the data's resolution).

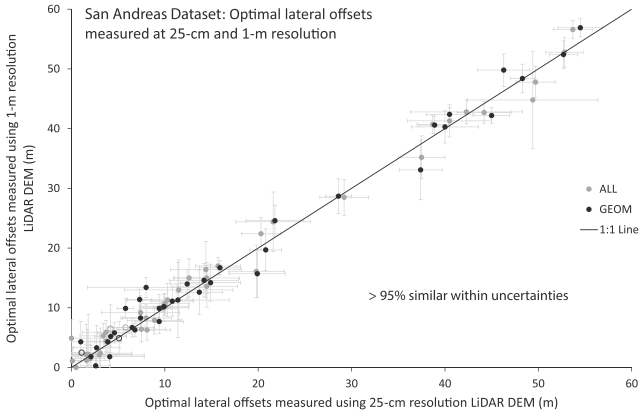

Figure 11. Comparison of the optimal lateral offsets measured across the 44 San Andreas markers using Lidar data at 25 cm and at 1 m resolution. Data are in Tables ES-A (25 cm resolution) and ES-B (1 m resolution).

Finally, Figure 11 compares the optimal lateral offsets obtained using Lidar data at 25 cm and at 1 m. The offsets are similar within uncertainties in more than 95% of the cases. A few short markers, however, generally less than 10–12 m long (on one or both sides of the fault), could not be resolved well in the 1 m data (uncertainties larger than the offset).

5. Application of 3D_Fault_Offsets to Measure Lateral and Vertical Offsets on Owens Valley (USA) and Hope (New Zealand) Faults

We apply 3D_Fault_Offsets to two other marker collections with prior offset measurements to better explore the potential of the code to identify and measure geomorphic markers in different tectonic and geomorphic contexts. We also aim to compare our vertical offsets to prior estimates. Measurements have been done as in section 4. The acronyms AUTO, CLICK, ALL, and GEOM are used similarly.

5.1. Owens Valley Fault Markers

The Owens Valley fault (USA) is a NNW-trending, ~80°NE dipping, ~140 km long, right-lateral, seismogenic strike-slip fault with a normal component (e.g., Beanland & Clark, 1994). Lidar data are available on the fault (www.opentopography.com, EarthScope Southern & Eastern California LiDAR Project), with a possible pixel size of ~25 cm (Haddon et al., 2016). Using the updated version v2 of the LaDiCaoz code, Haddon et al. (2016) have remotely measured the lateral and vertical offsets of 238 geomorphic markers across the fault, most being stream channels. The particularity of these markers is that many of them have low imprints in the topography, which the Lidar data hardly capture (see examples in supporting information ES4a). These subtle traces thus pose an interesting challenge for offset measurements.

We remeasured the lateral and vertical offsets of 20 of those markers (measurements in Table ES-C) chosen to be those having both prior and remote offset measurements, lateral and vertical wherever possible. Eight of them had been qualified as high quality, seven as moderate quality, and five as low quality (Haddon et al., 2016). Their available lateral and vertical offsets range between ~2–35 and ~0–6 m, respectively.

In the following, we have traced the fault as Haddon et al. (2016), considered a constant NE dip of 80 ± 10° at each site, and adopted conservative errors on both the DEM (pixel size of 1 m and vertical error of 0.5 m) and the fault position (assigned horizontal and vertical errors of 5 and 0.5 m, respectively). We discarded regressions with less than 10 points. We have used polygons of similar lengths to the marker sections considered by Haddon et al. (2016) (polygons referred to as "AsH"). Only four markers were long enough to run a second calculation with longer polygons (Table ES-C). In total, we have made 38 series of measures, representing a total of 684 lateral and vertical offset measures.

First, despite their subtle traces, 3D_Fault_Offsets well identifies the 20 markers as they had been identified earlier. In particular, the automatic extraction of their riverbeds is straightforward, with a 100% success rate (Figure 7c, Table ES-C, and examples in supporting information ES4a). The code also well identifies (i.e., with geomorphic relevance) one or both steepest slopes of the stream risers (~55 to 85%, Figure 7c). The top risers are geomorphically well defined in 25–35% of cases, whereas the measured riser bases and zones of maximum elevation more rarely have a geomorphic significance. When the few clearest outliers are manually removed, the above results are enhanced, with a better definition of the riser tops and bases.

As for the San Andreas data set, the mean lateral and vertical offsets obtained from the nine measurements (ALL) and from the geomorphically relevant measurements only (GEOM) are consistent, whether they were measured using AsHad or Longer polygons, and from the AUTO or CLICK approaches (Figure ES2_K in supporting information ES2). Therefore, the ALL and GEOM optimal offsets are also consistent, as shown in Figures 9c and 9d.

About 60% of our optimal geomorphic lateral offsets are similar within uncertainties to prior field measures (Figure 10d), whereas similarity with prior remote offsets from Haddon et al. (2016) occurs in ~70% of cases (Figure 10c). For vertical offsets, the population of field measures is small (seven measures), hampering any

robust comparison. Currently, similarity between prior vertical field offsets and our optimal vertical offsets is only in 43% of cases (Figure 10f). By contrast, our optimal vertical offsets compare well to the remote vertical offsets of Haddon et al. (2016), with similarity in 75% of the cases (Figure 10f).

The uncertainties on the calculated offsets are generally larger than prior propositions. While ~40 to 70% of the prior field and remote lateral offsets have been suggested to have uncertainties lower than 20% of the offset, about 40% of our optimal lateral offsets record the same ratio (Figure ES2_J(c) in supporting information ES2). With the exception of three poorly constrained lateral offsets (all $<$4 m), the optimal lateral slips are well constrained, however with uncertainties always less than 40% of the offset. The riverbeds have especially well constrained lateral offsets, with uncertainties lower than 20% of the offset in ~70% of the cases (Figure ES_J(c) in supporting information ES2). Errors previously reported on vertical offsets are also generally low, less than 20% of the offset in most cases (Figure ES2_J(d) in supporting information ES2), which contrasts with the common difficulty to measure small vertical offsets in the field and in topographic data. Uncertainties on a number of prior remote offsets are larger, however. The optimal vertical offsets measured here have uncertainties generally less than 40% of the offset, but this ratio is exceeded for the majority of vertical offsets less than 1 m.

5.2. Hope Fault Markers

The Hope fault (New Zealand) is an ENE-trending, NW-dipping (~70°), ~230 km long, seismogenic, strike-slip fault with a reverse component (e.g., Cowan & McGlone, 1991; Freund, 1971; Langridge & Berryman, 2005; Van Dissen & Yeats, 1991). Lidar data have been acquired on a 30 km long section of the eastern part of the fault (Manighetti, Perrin, et al., 2015), with a pixel size of 1 m and a vertical resolution of 10–20 cm. Using these remote data, Manighetti, Perrin, et al. (2015) have identified $>$200 markers and measured their lateral offsets from visual inspection of the back slipped marker traces in map view.

Most analyzed markers are stream channels and alluvial terrace risers. Their greatest particularity is that their trace is significantly weathered due to fast erosion in this region (e.g., Bull, 1991; Manighetti, Perrin, et al., 2015; O'Loughlin & Pearce, 1982). Furthermore, many of the markers are covered with vegetation that masks parts of their traces (e.g., Langridge et al., 2014). Therefore, the weathered and vegetated traces of the geomorphic markers across the Hope fault offer new challenging conditions for 3D_Fault_Offsets applications.

We remeasured the lateral offsets of 22 of those markers (82% are stream channels and 18% terrace risers or scarp edges of small reliefs), while measuring for the first time their vertical offsets. We have focused on markers offset by small amounts (most between ~2 and 40 m) to better test the potential of the code in these challenging conditions. Based on the degree of preservation of their geomorphic trace, 12, 8, and 2 of the markers were qualified as high, moderate, and low quality, respectively (Table ES-D; Manighetti, Perrin, et al., 2015).

In the following, we have traced the fault as Manighetti, Perrin, et al. (2015), considered a NW dip of 70 ± 10° at each site, and adopted conservative errors on both the DEM (pixel size of 1 m and vertical error of 1 m) and the fault position (assigned horizontal and vertical errors of 5 and 1 m, respectively). The acronyms AUTO, CLICK, ALL, and GEOM are used as before. In total, we have made 45 series of measures, representing a total of 810 lateral and vertical offset measures.

In 90% of the markers that are stream channels, the code succeeded to identify the riverbed well in a geomorphic sense (Figure 7d). It also identified well the steepest slopes and tops of the risers and scarps. When the clearest outliers are manually removed (CLICK), the bases of the risers and scarps also represent well the actual geomorphic properties of the markers. As for San Andreas and Owens Valley markers, only the zones of maximum elevation rarely have a geomorphic meaning.

As for the San Andreas and Owens data set, the mean lateral and vertical offsets obtained from the nine measurements (ALL) and from the geomorphically relevant measurements only (GEOM) are consistent, whether they were measured using the AUTO or CLICK approaches (Figure ES2_L in supporting information ES2). Therefore, the ALL and GEOM optimal offsets are also consistent, as shown in Figures 9e and 9f.

In 91% of cases, the optimal lateral offsets measured here are similar within uncertainties to the prior remote measures (Figure 10e). The uncertainties on the optimal offsets are also similar to prior estimates, less than 40% of the offset in the majority of cases (Figure ES2_J(e) in supporting information ES2). Two small lateral

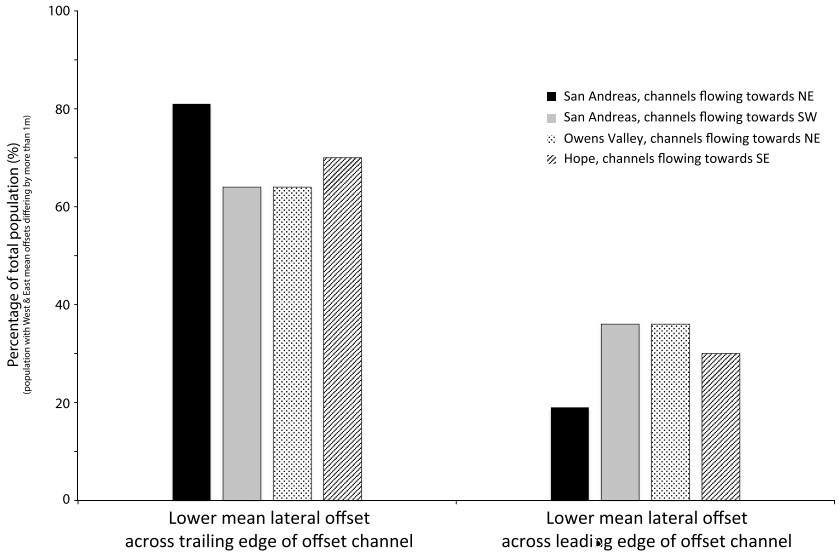

Figure 12. Histogram showing the percentage of channel markers in the three data sets that have a lower mean lateral offset across their trailing or their leading edge. See text.

offsets (<4 m) are poorly constrained with an uncertainty larger than the offset. The riverbed lateral offsets are the best constrained, with ~60% of them having an uncertainty less than 20% of the slip. This shows that riverbeds well record the lateral offsets.

The vertical offsets we measured are low, less than 2 m for the majority of them, with a maximum of ~4 m. As expected from the DEM resolution and the conservative vertical errors we input in the calculations, these low vertical offsets have large uncertainties, and the smallest ones (<1–1.5 m) are not properly resolved (uncertainty similar or greater than the offset, Figures ES2_J(f and f_{bis}) in supporting information ES2).

6. Discussion

Of the 88 fault offset geomorphic markers that we analyzed, 3D_Fault_Offsets succeeded to mathematically identify 87 of them, and to measure their lateral and vertical offsets, along with their uncertainties. Overall, the measured offsets compare well to the prior estimates—field and remote. This agreement confirms that 3D_Fault_Offsets may efficiently assist the slip measurements along faults. It also provides new opportunities.

6.1. Opportunity to Examine the Preservation of Lateral Offsets Across the Entirety of Markers

Because 3D_F
ault_Offsets measures the lateral offset of a marker potentially utilizing nine of its intrinsic geometric features, it offers the opportunity to examine the variability of the lateral offset preservation across the entirety of the marker. If the latter is a stream channel, this makes it possible to examine the preservation of the lateral offset across its "western" and "eastern" (here defined on code-rotated attitudes) risers. We have thus calculated the mean lateral offsets across the western and the eastern risers of the channel markers and analyzed their peak value that represents the most robustly constrained offset. Details can be found in supporting information ES5.

For 70% of the San Andreas stream channels, the west and east riser lateral offsets differ by more than 1 m, that is, more than four pixels, and thus, this difference is significant. About 80% of the channels flowing toward the NE have their western mean lateral offset lower than their eastern mean offset by more than 1 m (Figure 12). About 64% of the channels flowing toward the SW have their eastern mean lateral offset lower than their western offset by more than 1 m (Figure 12). This suggests that the preservation of the lateral offsets across the channels is partly dependent on their flow direction. Across channels flowing toward the NE, the dextral motion of the San Andreas Fault likely leads to the greater trimming of the channel's western trailing edge (trailing edge defined in downstream side of fault), because the channel tends to minimize the lateral translation of its bed (see sketch in supporting information ES5). Across channels flowing toward the

SW, a similar tendency of channels to minimize the lateral deviation of their bed leads to the trimming of their eastern trailing edge.

Similarly, about 65% of the Owens Valley channels flowing toward the NE have their western mean lateral offset, hence the offset across their trailing edge, lower than their eastern mean offset by more than 1 m (Figure 12). About 70% of the Hope channels flowing toward the SE have their eastern mean lateral offset, hence the offset across their trailing edge, lower than their western mean offset by more than 1 m (Figure 12).

Trimming of channel trailing edges is thus common along the three faults. While these relations between stream channel flow and sense of fault motion have been discussed for a long time (e.g., McCalpin, 2009; McGill & Sieh, 1991; Wallace, 1990), 3D_Fault_Offsets provides a new opportunity to document them and to quantify the degree of trimming and of preservation of the lateral offsets across the entirety of channel markers.

6.2. Opportunity to Examine the Preservation of Vertical Offsets Across the Entirety of Markers

The rich offset record also offers the opportunity to examine the preservation of the vertical offset across the entirety of the marker. First, contrary to lateral offsets (Figure ES2_J in supporting information ES2), errors on riverbed vertical offsets are not systematically lower than those on western and eastern mean vertical offsets (Series A2 of figures in supporting information ES5). This shows that riverbeds are systematically not the geomorphic features to best preserve the vertical offsets. Second, no relation seems to exist between the direction of channel flow, the trimming of either riser, and their vertical offsets. Laterally trimmed risers do not have lower vertical offsets than more preserved edges or beds. In about 60% of the San Andreas stream channels, the riverbed vertical offset differs from that of one or both risers by more than 50 cm (3–5 times the vertical resolution). Generally (~70%), the riverbed has a lower vertical offset than the risers. A reasonable interpretation is that, as a channel goes on flowing after its bed has been vertically offset by the fault motion, it incises the uplifted compartment and hence partly trims the vertical offset, tending to attain a mostly continuous longitudinal profile (Ouchi, 2004). By contrast, the two risers are better preserved and hence retain the record of the actual vertical offset better.

The Owens Valley data are too few to examine this issue (Series B2 of figures in supporting information ES5), but 75% of the cases where the riverbed vertical offset differs by more than 50 cm from that of one or both risers are such that the vertical offset preserved by the riverbed is lower than the one preserved by one or both risers. This figure is 76% for Hope channel cases (Series C2 of figures in supporting information ES5). Together these confirm that the riverbeds are not the geomorphic features that best preserve the vertical offsets; those should rather be measured across the flanking risers.

The vertical back slips performed by the code allow the user to examine the plausible vertical reconstructions of the up to nine geomorphic features (see Figure 6 and supporting information ES6, where these reconstructions are shown for the San Andreas markers). The vertical back slip plots confirm that the riverbeds are well identified. Even though they do not generally preserve the entirety of the net vertical offset, they preserve a clear geomorphic signature of the fault vertical motion. The riser steepest slopes are also generally well defined, and their vertical offsets seem to be a fair estimate of the actual net vertical offset across the marker. In many cases, the riser tops are also well defined in the *Z* dimension and hence provide a relevant record of the vertical offset. The riser bases are generally more poorly constrained. While they are generally not shown on figures of supporting information ES6, because they have no clear geomorphic meaning, the maximum elevation point clouds are expected to provide an accurate record of the net cumulative vertical offset across the markers.

The vertical reconstructions also allow for examining what the original morphology of a marker might have looked like in the vertical dimension. If two marker sections have been incorrectly paired based on the examination of their horizontal traces, the vertical reconstructions should help to detect it (see possible example Sieh145 in supporting information ES3).

6.3. Opportunity to Estimate the Vertical to Lateral Slip Ratios

Estimating the ratio between lateral and vertical slip on a strike-slip fault is commonly a challenge because vertical offset measurements are few and possibly small. Yet this information is important to understand

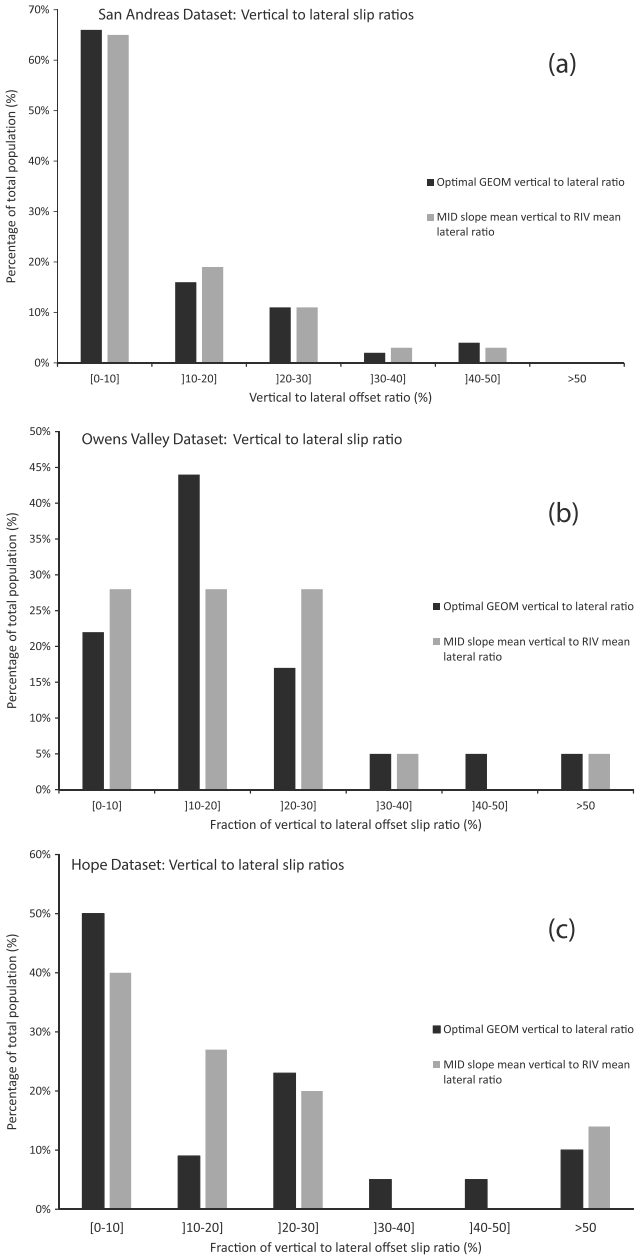

Figure 13. Vertical to lateral slip ratios measured in the three data sets. The ratios are calculated from both the optimal geomorphic offsets (GEOM) and the mean vertical and lateral offsets recorded by the steepest slopes and the riverbeds, respectively.

the kinematics of the fault, the way slip is partitioned on its different segments and branches, and to anticipate the amount of vertical slip that might be expected during a large earthquake on the fault.

3D_Fault_Offsets allows for estimating the ratio of vertical to lateral slip in any series of measurements. For reasons discussed earlier, the steepest slopes are believed to best preserve the net vertical offset, whereas the riverbeds best record the lateral offsets. Therefore, Figure 13 shows the vertical to lateral slip ratios calculated in the three data sets both from the midslope vertical and the riverbed lateral offsets and from the geomorphic optimal vertical and lateral offsets. The San Andreas Fault is the one to have the lowest vertical slip component, in effect showing vertical to lateral slip ratios lower than 10% in almost 70% of the analyzed markers (Figure 13a). The other two faults, Owens Valley and Hope have greater vertical to lateral slip ratios, with ~85% of their total population having a vertical component equal to 10 to 30% of the lateral offset (Figures 13b and 13c). This larger fraction of vertical slip is consistent with the two faults having a clear dip-slip component, normal for Owens Valley and reverse for Hope. The vertical to lateral slip ratios found for the Owens Valley fault are consistent with prior estimates (Haddon et al., 2016). By contrast, those found for the Hope fault are larger than previously proposed (~10%, e.g., Cowan & McGlone, 1991; Berryman et al., 1992; Langridge & Berryman, 2005).

6.4. Uncertainties on Lateral and Vertical Offsets

One important issue emphasized from 3D_Fault_Offsets is the significance of the uncertainties on the measured offsets. Several sources of errors are revealed. The first is related to a possible incorrect identification of the two marker sections to be paired (e.g., Mackenzie & Elliott, 2017; Scharer et al., 2014; Zielke et al., 2015). The expertise of the user is here fundamental and irreplaceable. However, 3D_Fault_Offsets may assist the user in this identification phase, especially when stream channels are concerned, since it indicates from its very first routine F1 whether it succeeds in identifying the riverbed. A failure to provide this identification may suggest that the proposed marker is not a robust feature. Later on, the success of the code to characterize other geometrical properties of the suggested marker is a further support, or lack of support, of its existence and geomorphic relevance.

Once two paired marker sections are properly identified and their section to be matched well defined, a second source of error is analytical. As we discussed it in sections 2 and 3, multiple sources of errors combine. While the same multiple errors exist in the field measurements of fault offsets, they are rarely accounted for and the uncertainties provided restrict to the range of reconstructions of the marker trace in map view that the user visually estimates as being plausible. Obviously, the actual sources of errors are much more numerous, and the resulting uncertainties are expected to be larger than generally proposed. In most of the measurements we performed, we indeed found errors significantly larger than previously suggested in the field measurements. The LaDiCaoz code was a first attempt to better quantify the errors on the lateral (Zielke et al., 2012) and vertical (Haddon et al., 2016) offsets of sublinear features, but this quantification still included some simplifications that led to smaller errors than those we derive, even though they were greater than field estimates.

As we discussed in sections 2 and 3, 3D_Fault_Offsets may retain certain outlier points of different origins that may introduce an additional error on the offset estimates. However, the density of outliers points is generally low (attested by consistency between AUTO and CLICK measures; see Figure 8b), while the irrelevant offset

calculations are smoothed out in the overall statistical analysis of the results (attested by consistency between ALL and GEOM measures; see Figure 9). Therefore, the outlier points and the misleading best fitting regressions that 3D_Fault_Offsets may produce do not alter the final offset measures and hardly increase their uncertainties.

Another source of uncertainty on the offset measures relates to the length of each marker section to be correlated. Because the original geometry of the marker is unknown, the selection of the two marker sections to be paired is disputable in every marker case, especially those with a complex trace (e.g., Zielke et al., 2015). The lateral and vertical offset values measured with 3D_Fault_Offsets vary with the length of the paired marker sections, even if not dramatically in the cases analyzed here (see Figure 8c). Therefore, there exists a variability in the offset measures and hence an additional uncertainty that is related to the user definition of the original prefaulted geometry of the marker. While 3D_Fault_Offsets cannot recognize which marker sections best represent the original trace of a marker, it allows for producing a series of measures made to integrate the full range of plausible lengths, and as such, it allows for estimating the offset uncertainties related to the marker geometry. Generally, it seems beneficial to take a fairly long section of a marker, especially when the latter is sinuous (i.e., meandering), so as to smooth out the marker irregularities and create an average morphology.

We have shown in sections 6.1 and 6.2 that the preservation of the lateral and of the vertical offsets generally differs across the marker. While the lateral offset is generally well preserved across the riverbed, it may be partly trimmed across one or both risers due to the combination of channel flow and fault motion. Conversely, while the vertical offset is generally well preserved across one or both of its risers, it is commonly trimmed in the riverbed. Therefore, an additional uncertainty affects the offsets, which relates to the geomorphic feature(s) across which they are measured. When the offset is averaged across all geomorphic features that characterize a marker, the uncertainties are large (Figure ES2_J in supporting information ES2), partly due to the intrinsic variability of the offset preservation across the marker. When the variability of the offset cannot be confidently related to trimming or to any other well-understood process, the offset averaged across the entirety of the marker should be considered, along with its large uncertainties. When evidence for trimming (or for any other clear process) is clear, the user might thoughtfully select the feature(s) that have best preserved the lateral or vertical offsets. This would refine the offset values and lower their uncertainties. Such a selection might be needed, for instance, when dense collections of offsets are statistically analyzed to recover earthquake slip increments (e.g., Manighetti, Perrin, et al., 2015). Meanwhile, the variability of the offset across the marker may contribute to quantify the trimming.

In the present study, we have analyzed small offsets, less than a few tens of meters. Would the offsets be much larger, the geometry of the fault plane could induce another source of variability in the measured offsets that would need to be taken into account (e.g., Mackenzie & Elliott, 2017).

Finally, the proper functioning of 3D_Fault_Offsets relies on a balance between the DEM resolution, the length of the markers to be analyzed, and the height of their vertical imprint. If the latter is too small, at the limit of the DEM vertical resolution, corduroy or any other noise in the Lidar data may prevent the fair identification of the marker. If the marker is very short, the topographic data points might be too few to allow for its identification. From the measurements we have performed here, we suggest that 3D_Fault_Offsets needs a minimum of one topographic data point per meter to identify short markers no longer than ~10 m (on one or both sides of the fault). Topographic data at a resolution greater than 1 m are thus needed to analyze very short markers. Conversely, if the markers under concern are longer than 10–15 m (on each side of the fault), Lidar data at 1 m resolution are appropriate to identify and measure them well. They might even be preferred to higher resolution topographic data for the latter generally introduce noise that may interfere with the point identification (compare resolutions in Figure 5 and ES1_C).

7. Conclusions

We have developed a new Matlab code, 3D_Fault_Offsets, to automate fault slip measurements across offset sublinear geomorphic markers. The code uses topographic data and remotely measures the lateral and vertical offsets of the topographic 3-D traces of the markers, as they express prominent sublinear geomorphic characters such as riverbed, base, middle and top of risers or scarps, and crests or ridges. The code requires only a small amount of user interaction. It thus limits most of the possible bias that are commonly associated

with fault offset measurements (e.g., Scharer et al., 2014), especially with the assigned uncertainties (i.e., offset ranges). We tested the code successfully on three sets of markers (88 at total) offset by different faults, San Andreas, Owens Valley, and Hope. The success of 3D_Fault_Offsets was attested by its ability to reproduce previously made measurements along those faults, providing in the largest number of cases offset estimates that are within the uncertainties of the previous measurements. This successful test indicates that 3D_Fault_Offsets is working well. Considering the quickly growing number of high-resolution topographic data sets (e.g., Opentopography website, e.g., Bemis et al., 2014; Johnson et al., 2014) and the anticipated, corresponding growth of the number of studies that perform fault offset measurements, including earthquake slip measures (e.g., Zielke et al., 2015), 3D_Fault_Offsets might be beneficial to a wide range of researchers in the field. Additionally, the largely "hands-off" approach of the code makes the offset measurements not only faster (more than 5,000 offset measurements were performed here) but also more reliable and reproducible.

In addition to lateral offsets, 3D_Fault_Offsets provides a systematic and rich compilation of the vertical offsets. This opens new opportunities to examine the different slip components and their ratios on the faults (see also Billant et al., 2016; Mackenzie & Elliott, 2017), as the relations between alluvial dynamics and fault motion (e.g., Ouchi, 2005). 3D_Fault_Offsets also provides a means to quantify the trimming of the channel banks that results from the combination of alluvial dynamics and lateral fault slip. These insights might be useful to estimate the erosion conditions and the relative age of the lateral offsets.

While 3D_Fault_Offsets cannot determine the relevance of matching two marker sections, it allows for the quantitative comparison of these two sections and hence the examination of the geomorphic relevance of their pairing. It might also allow for the measurement of the morphological complexities of the markers that may exist due to their warping, deflection, tilting, distributed faulting, etc. in the fault vicinity (e.g., Ouchi, 2005). Therefore, 3D_Fault_Offsets offers an efficient assistance to the geologists willing to analyze fault and marker morphology and to measure a large collection of offsets. As for any remote measurements, the marker identification performed by 3D_Fault_Offsets may gain confidence if cross-checked with field observations. However, the tremendous amount of offset measures the code produces goes much beyond the possibilities of field measurements.

Finally, 3D_Fault_Offsets can be run with any fault dip, and therefore, it should be applicable to dip-slip faults. The only condition is that distinguishable geomorphic markers must exist that are vertically offset by the fault. This might be the case, for instance, for perched streambeds on top of normal fault footwalls (e.g., Monaco et al., 1997).

Acknowledgments

The Lidar data used in the present study can be found on www.opentopography.org (B4 LiDAR Project and EarthScope Southern & Eastern California LiDAR Project) and in the prior papers that published them (Zielke et al., 2012; Haddon et al., 2016; Manighetti, Perrin, et al., 2015). The measurement data sets produced in the present study are available in the supporting information. This work has been funded by Université Côte d'Azur, Nice, France. We greatly thank the two reviewers (O. Zielke and O. Bellier) and the Associate Editor for their thorough constructive comments that greatly helped us to improve our manuscript.

References

Ansberque, C., Bellier, O., Godard, V., Lasserre, C., Wang, M., Braucher, R., … Bourlès, D. L. (2016). The Longriqu fault zone, eastern Tibetan Plateau: Segmentation and Holocene behavior. *Tectonics*, *35*, 565–585. https://doi.org/10.1002/2015TC004070

Armijo, R., Tapponnier, P., & Han, T. (1989). Late Cenozoic right-lateral strike-slip faulting in southern Tibet. *Journal of Geophysical Research*, *94*, 2787–2838. https://doi.org/10.1029/JB094iB03p02787

Arrowsmith, J. R., & Zielke, O. (2009). Tectonic geomorphology of the San Andreas Fault zone from high resolution topography: An example from the Cholame segment. *Geomorphology*, *113*(1-2), 70–81. https://doi.org/10.1016/j.geomorph.2009.01.002

Beanland, S., & Clark, M. M. (1994). The Owens Valley fault zone, eastern California, and surface faulting associated with the 1872 earthquake (no. 1982). U.S. Geological Survey.

Beauprêtre, S., Garambois, S., Manighetti, I., Malavieille, J., Sénéchal, G., Chatton, M., … Romano, C. (2012). Finding the buried record of past earthquakes with GPR-based palaeoseismology: A case study on the Hope fault, New Zealand. *Geophysical Journal International*, *189*(1), 73–100. https://doi.org/10.1111/j.1365-246X.2012.05366.x

Beauprêtre, S., Manighetti, I., Garambois, S., Malavieille, J., & Dominguez, S. (2013). Stratigraphic architecture and fault offsets of alluvial terraces at Te Marua, Wellington fault, New Zealand, revealed by pseudo-3D GPR investigation. *Journal of Geophysical Research: Solid Earth*, *118*, 4564–4585. https://doi.org/10.1002/jgrb.50317

Bemis, S. P., Micklethwaite, S., Turner, D., James, M. R., Akciz, S., Thiele, S. T., & Bangash, H. A. (2014). Ground-based and UAV-based photogrammetry: A multi-scale, high-resolution mapping tool for structural geology and paleoseismology. *Journal of Structural Geology*, *69*, 163–178. https://doi.org/10.1016/j.jsg.2014.10.007

Berryman, K. R., Beanland, S., Cooper, A. F., Cutten, H. N., Norris, R. J., & Wood, P. R. (1992). The Alpine Fault, New Zealand: Variation in Quaternary structural style and geomorphic expression. *Annales Tectonicae*, *6*, 126–163.

Bevis, M., Hudnut, K., Sanchez, R., Toth, C., Grejner-Brzezinska, D., Kendrick, E., … & Shindle, W. (2005). The B4 project: Scanning the San Andreas and San Jacinto fault zones. Abstract H34B-01 Presented at the 2005 AGU Fall Meeting, San Francisco, CA.

Billant, J., Bellier, O., Godard, V., & Hippolyte, J.-C. (2016). Constraining recent fault offsets with statistical and geometrical methods: Example from the Jasneuf fault (Western Alps, France). *Tectonophysics*, *693*, 1–21. https://doi.org/10.1016/j.tecto.2016.09.031

Bull, W. B. (1991). *Geomorphic responses to climate change*. New York: Oxford University Press.

Burbank, D. W., & Anderson, R. S. (2011). *Tectonic geomorphology*. Chichester, UK: John Wiley. https://doi.org/10.1002/9781444345063

Cowan, H. A., & McGlone, M. S. (1991). Late Holocene displacements and characteristic earthquakes on the Hope River segment of the Hope fault. *New Zealand Journal of the Royal Society*, *21*(4), 285–293.

De Pascale, G. P., Quigley, M. C., & Davies, T. R. H. (2014). Lidar reveals uniform Alpine fault offsets and bimodal plate boundary rupture behavior, New Zealand. *Geology*, *42*(5), 411–414. https://doi.org/10.1130/G35100.1

Frankel, K. L., Dolan, J. F., Finkel, R. C., Owen, L. A., & Hoeft, J. S. (2007). Spatial variations in slip rate along the Death Valley-Fish Lake Valley fault system determined from LiDAR topographic data and cosmogenic Be-10 geochronology. *Geophysical Research Letters*, *34*, L18303. https://doi.org/10.1029/2007GL030549

Freund, R. (1971). The Hope fault: A strike-slip fault in New Zealand. *New Zealand Geological Survey Bulletin*, *86*, 49.

Gaudemer, Y., Tapponnier, P., Meyer, B., Peltzer, G., Shunmin, G., Zhitai, C., … Cifuentes, I. (1995). Partitioning of crustal slip between linked, active faults in the eastern Qilian Shan, and evidence for a major seismic gap, the 'Tianzhu gap', on the western Haiyuan Fault, Gansu (China). *Geophysical Journal International*, *120*(3), 599–645. https://doi.org/10.1111/j.1365-246X.1995.tb01842.x

Gaudemer, Y., Tapponnier, P., & Turcotte, D. (1989). River offsets across active strike-slip faults. *Annales Tectonicae*, *3*(3), 55–76.

Gold, R., Cowgill, E., Arrowsmith, J. R., Chen, X., Sharp, W. D., Cooper, K. M., & Wang, X. F. (2011). Faulted terrace risers place new constraints on the late Quaternary slip rate for the central Altyn Tagh Fault, northwest Tibet. *Geological Society of America Bulletin*, *123*(5-6), 958–978. https://doi.org/10.1130/B30207.1

Gold, R. D., Cowgill, E., Arrowsmith, J. R., Gosse, J., Chen, X., & Wang, X.-F. (2009). Riser diachroneity, lateral erosion, and uncertainty in rates of strike-slip faulting: A case study from Tuzidun along the Altyn Tagh Fault, NW China. *Journal of Geophysical Research*, *114*, B04401. https://doi.org/10.1029/2008JB005913

Haddad, D. E., Akçiz, S. O., Arrowsmith, J. R., Rhodes, D. D., Oldow, J. S., Zielke, O., … Shilpakar, P. (2012). Applications of airborne and terrestrial laser scanning to paleoseismology. *Geosphere*, *8*(4), 771–786. https://doi.org/10.1130/GES00701.1

Haddon, E. K., Amos, C. B., Zielke, O., Jayko, A. S., & Bürgmann, R. (2016). Surface slip during large Owens Valley earthquakes. *Geochemistry, Geophysics, Geosystems*, *17*, 2239–2269. https://doi.org/10.1002/2015GC006033

Hubert-Ferrari, A., Armijo, R., King, G., Meyer, B., & Barka, A. (2002). Morphology, displacement, and slip rates along the north Anatolian fault, Turkey. *Journal of Geophysical Research*, *107*(B10), 2235. https://doi.org/10.1029/2001JB000393

Johnson, K., Nissen, E., Saripalli, S., Arrowsmith, J. R., McGarey, P., Scharer, K., … Blisniuk, K. (2014). Rapid mapping of ultrafine fault zone topography with structure from motion. *Geosphere*, *10*(5), 969–986. https://doi.org/10.1130/GES01017.1

Klinger, Y., Etchebes, M., Tapponnier, P., & Narteau, C. (2011). Characteristic slip for five great earthquakes along the Fuyun fault in China. *Nature Geoscience*, *4*(6), 389–392. https://doi.org/10.1038/ngeo1158

Knuepfer, P. L. K. (1987). Changes in Holocene slip rates in strike-slip environments, U.S. Geol. Surv. Open File Rep. 249–261.

Langridge, R. M., & Berryman, K. R. (2005). Morphology and slip rate of the Hurunui section of the Hope fault, South Island, New Zealand. *New Zealand Journal of Geology and Geophysics*, *48*(1), 43–57. https://doi.org/10.1080/00288306.2005.9515097

Langridge, R. M., Ries, W. F., Farrier, T., Barth, N. C., Khajavi, N., & De Pascale, G. P. (2014). Developing sub 5-m LiDAR DEMs for forested sections of the Alpine and Hope faults, South Island, New Zealand: Implications for structural interpretations. *Journal of Structural Geology*, *64*, 53–66. https://doi.org/10.1016/j.jsg.2013.11.007

Lasserre, C., Morel, P.-H., Gaudemer, Y., Tapponnier, P., Ryerson, F. J., King, G., … Yong, D. (1999). Post-glacial left slip-rate and past occurrence of $M \geq 8$ earthquakes on the western Haiyuan fault (Gansu, China). *Journal of Geophysical Research*, *104*, 17,633–17,651. https://doi.org/10.1029/1998JB900082

Lensen, G. (1968). Analysis of progressive fault displacements during downcutting at the Branch River terraces, South Island. *Geological Society of America Bulletin*, *79*(5), 545–566. https://doi.org/10.1130/0016-7606(1968)79%5B545:AOPFDD%5D2.0.CO;2

Lensen, G. J. (1964). The general case of progressive displacement of flights of degradational terraces. *New Zealand Journal of Geology and Geophysics*, *7*(4), 864–870. https://doi.org/10.1080/00288306.1964.10428134

Li, H., Van der Woerd, J., Sun, Z., Si, J., Tapponnier, P., Pan, J., … Chevalier, M. L. (2012). Co-seismic and cumulative offsets of the recent earthquakes along the Karakax left-lateral strike-slip fault in western Tibet. *Gondwana Research*, *21*(1), 64–87. https://doi.org/10.1016/j.gr.2011.07.025

Lienkaemper, J. J. (2001). 1857 slip on the San Andreas Fault southeast of Cholame, California. *Bulletin of the Seismological Society of America*, *91*(6), 1659–1672. https://doi.org/10.1785/0120000043

Lin, Z., Kaneda, H., Mukoyama, S., Asada, N., & Chiba, T. (2013). Detection of subtle tectonic-geomorphic features in densely forested mountains by very high-resolution airborne LiDAR survey. *Geomorphology*, *182*, 104–115. https://doi.org/10.1016/j.geomorph.2012.11.001

Lowell, T. V. (1995). The application of radiocarbon age estimates to the dating of glacial sequences: An example from the Miami sublobe, Ohio, U.S.A. *Quaternary Science Reviews*, *14*(1), 85–99. https://doi.org/10.1016/0277-3791(94)00113-P

Ludwig, L. G., Akçiz, S. O., Noriega, G. R., Zielke, O., & Arrowsmith, J. R. (2010). Climate-modulated channel incision and rupture history of the San Andreas Fault in the Carrizo Plain. *Science*, *327*(5969), 1117–1119. https://doi.org/10.1126/science.1182837

Mackenzie, D., & Elliott, A. (2017). Untangling tectonic slip from the potentially misleading effects of landform geometry. *Geosphere*, *13*(4). https://doi.org/10.1130/GES01386.1

Manighetti, I., Campillo, M., Sammis, C., Mai, P. M., & King, G. (2005). Evidence for self-similar, triangular slip distributions on earthquakes: Implications for earthquake and fault mechanics. *Journal of Geophysical Research*, *110*, B05302. https://doi.org/10.1029/2004JB003174

Manighetti, I., Caulet, C., Barros, L., Perrin, C., Cappa, F., & Gaudemer, Y. (2015). Generic along-strike segmentation of Afar normal faults, East Africa: Implications on fault growth and stress heterogeneity on seismogenic fault planes. *Geochemistry, Geophysics, Geosystems*, *16*, 443–467. https://doi.org/10.1002/2014GC005691

Manighetti, I., King, G., & Sammis, C. (2004). The role of off-fault damage in the evolution of normal faults. *Earth and Planetary Science Letters*, *217*(3-4), 399–408. https://doi.org/10.1016/S0012-821X(03)00601-0

Manighetti, I., King, G. C. P., Gaudemer, Y., Scholz, C. H., & Doubre, C. (2001). Slip accumulation and lateral propagation of active normal faults in Afar. *Journal of Geophysical Research*, *106*, 13,667–13,696. https://doi.org/10.1029/2000JB900471

Manighetti, I., Perrin, C., Dominguez, S., Garambois, S., Gaudemer, Y., Malavieille, J., … Beauprêtre, S. (2015). Recovering paleoearthquake slip record in a highly dynamic alluvial and tectonic region (Hope fault, New Zealand) from airborne LiDAR. *Journal of Geophysical Research: Solid Earth*, *120*, 4484–4509. https://doi.org/10.1002/2014JB011787

McCalpin, J. P. (Ed.) (2009). *Paleoseismology*, *2nd Edition. International Geophysics Series* (Vol. 95, 647 pp.). Elsevier.

McGill, S. F., & Sieh, K. (1991). Surficial offsets on the central and eastern Garlock Fault associated with prehistoric earthquakes. *Journal of Geophysical Research*, *96*, 21,597–21,621. https://doi.org/10.1029/91JB02030

Meigs, A. (2013). Active tectonics and LiDAR revolution. *Lithosphere*, *5*(2), 226–229. https://doi.org/10.1130/RF.L004.1

Monaco, C., Tapponnier, P., Tortorici, L., & Gillot, P. Y. (1997). Late Quaternary slip rates on the Acireale-Piedimonte normal faults and tectonic origin of Mt. Etna (Sicily). *Earth and Planetary Science Letters*, *147*(1-4), 125–139. https://doi.org/10.1016/S0012-821X(97)00005-8

O'Loughlin, C. L., & Pearce, A. J. (1982). Erosion processes in the mountains. In J. M. Soons & M. J. Selby (Eds.), *Landforms of New Zealand* (pp. 67–79). Auckland: Longman Paul.

Ouchi, S. (2004). Flume experiments on the horizontal stream offset by strike-slip faults. *Earth Surface Processes and Landforms*, *29*(2), 161–173. https://doi.org/10.1002/esp.1017

Ouchi, S. (2005). Development of offset channels across the San Andreas Fault. *Geomorphology*, *70*(1-2), 112–128. https://doi.org/10.1016/j.geomorph.2005.04.004

Pazzaglia, F. J. (2013). 9.22 Fluvial terraces. In *Treatise on Geomorphology* (pp. 379–412). San Diego, CA: Academic Press.

Peltzer, G., Tapponnier, P., Gaudemer, Y., Meyer, B., Guo, S., Yin, K., … Dai, H. (1988). Offsets of late Quaternary morphology, rate of slip, and recurrence of large earthquakes on the Chang Ma Fault (Gansu, China). *Journal of Geophysical Research*, *93*, 7793–7812. https://doi.org/10.1029/JB093iB07p07793

Perrin, C., Manighetti, I., Ampuero, J.-P., Cappa, F., & Gaudemer, Y. (2016). Location of largest earthquake slip and fast rupture controlled by along-strike change in fault structural maturity due to fault growth. *Journal of Geophysical Research: Solid Earth*, *121*, 3666–3685. https://doi.org/10.1002/2015JB012671

Ren, Z., Zhang, Z., Chen, T., Yan, S., Yin, J., Zhang, P., … Li, C. (2016). Clustering of offsets on the Haiyuan fault and their relationship to paleoearthquakes. *Geological Society of America Bulletin*, *128*(1–2), 3–18.

Replumaz, A., Lacassin, R., Tapponnier, P., & Leloup, P. H. (2001). Large river offsets and Plio-Quaternary dextral slip rate on the Red River fault (Yunnan, China). *Journal of Geophysical Research*, *106*, 819–836. https://doi.org/10.1029/2000JB900135

Ritz, J. F., Brown, E. T., Bourles, D. L., Philip, H., Schlupp, A., Raisbeck, G. M., … Enkhtuvshin, B. (1995). Slip rates along active faults estimated with cosmic-ray-exposure dates: Application to the Bogd Fault, Gobi-Altaï, Mongolia. *Geology*, *23*(11), 1019–1022. https://doi.org/10.1130/0091-7613(1995)023%3C1019:SRAAFE%3E2.3.CO;2

Rizza, M., Ritz, J. F., Prentice, C., Vassallo, R., Braucher, R., Larroque, C., … ASTER Team (2015). Earthquake geology of the Bulnay Fault (Mongolia). *Bulletin of the Seismological Society of America*, *105*(1), 72–93. https://doi.org/10.1785/0120140119

Salisbury, J. B., Haddad, D. E., Rockwell, T. K., Arrowsmith, J. R., Madugo, C., Zielke, O., & Scharer, K. (2015). Validation of meter-scale surface faulting offset measurements from high-resolution topographic data. *Geosphere*, *11*(6), 1884–1901. https://doi.org/10.1130/GES01197.1

Salisbury, J. B., Rockwell, T. K., Middleton, T. J., & Hudnut, K. W. (2012). LiDAR and field observations of slip distribution for the most recent surface ruptures along the central San Jacinto Fault. *Bulletin of the Seismological Society of America*, *102*(2), 598–619. https://doi.org/10.1785/0120110068

Scharer, K. M., Salisbury, J. B., Arrowsmith, J. R., & Rockwell, T. K. (2014). Southern San Andreas Fault evaluation field activity: Approaches to measuring small geomorphic offsets—challenges and recommendations for active fault studies. *Seismological Research Letters*, *85*, 1.

Yeats, R. S., Sieh, K., & Allen, C. R. (1997). *The geology of earthquakes* (568 pp.). New York: Oxford University Press.

Sieh, K. E. (1978). Slip along the San Andreas Fault associated with the great 1857 earthquake. *Bulletin of the Seismological Society of America*, *68*(5), 1421–1448.

Sieh, K. E. (1984). Lateral offset and revised dates of large prehistoric earthquakes at Pallett Creek, southern California. *Journal of Geophysical Research*, *89*, 7641–7670. https://doi.org/10.1029/JB089iB09p07641

Tapponnier, P., Ryerson, F. J., Van der Woerd, J., Mériaux, A.-S., & Lasserre, C. (2001). Long-term slip rates and characteristic slip: Keys to active fault behaviour and earthquake hazard. *Earth and Planetary Science Letters*, *333*, 483–494.

Van der Woerd, J., Ryerson, F. J., Tapponnier, P., Gaudemer, Y., Finkel, R., Mériaux, A. S., … He, Q. (1998). Holocene left slip-rate determined by cosmogenic surface dating on the Xidatan segment of the Kunlun fault (Qinghai, China). *Geology*, *26*(8), 695–698. https://doi.org/10.1130/0091-7613(1998)026%3C0695:HLSRDB%3E2.3.CO;2

Van der Woerd, J., Tapponnier, P., Ryerson, F. J., Meriaux, A.-S., Meyer, B., Gaudemer, Y., … Zhiqin, X. (2002). Uniform postglacial slip-rate along the central 600 km of the Kunlun Fault (Tibet), from 26Al, 10Be, and 14C dating of riser offsets, and climatic origin of the regional morphology. *Geophysical Journal International*, *148*(3), 356–388. https://doi.org/10.1046/j.1365-246x.2002.01556.x

Van Dissen, R., & Yeats, R. S. (1991). Hope fault, Jordan thrust, and uplift of the seaward Kaikoura range, New Zealand. *Geology*, *19*(4), 393–396. https://doi.org/10.1130/0091-7613(1991)019%3C0393:HFJTAU%3E2.3.CO;2

Wallace, R. E. (1968). Notes on stream channels offset by the San Andreas Fault, southern coast ranges, California. In W. R. Dickinson & A. Grantz (Eds.), *Proc. of Conf. on geologic problems of the San Andreas Fault System*, *Stanford University Publications in the Geological Sciences* (Vol. 11, pp. 6–21). Stanford, California: Stanford University.

Wallace, R. E. (1990). Geomorphic expression. *The San Andreas Fault System, California*, *1515*, 14–58.

Zechar, J. D., & Frankel, K. L. (2009). Incorporating and reporting uncertainties in fault slip rates. *Journal of Geophysical Research*, *114*, B12407. https://doi.org/10.1029/2009JB006325

Zielke, O., & Arrowsmith, J. R. (2012). LaDiCaoz and LiDARimager—MATLAB GUIs for LiDAR data handling and lateral displacement measurement. *Geosphere*, *8*(1), 206–221. https://doi.org/10.1130/GES00686.1

Zielke, O., Arrowsmith, J. R., Ludwig, L. G., & Akçiz, S. O. (2010). Slip in the 1857 and earlier large earthquakes along the Carrizo Plain, San Andreas Fault. *Science*, *327*(5969), 1119–1122. https://doi.org/10.1126/science.1182781

Zielke, O., Arrowsmith, J. R., Ludwig, L. G., & Akciz, S. O. (2012). High-resolution topography-derived offsets along the 1857Fort Tejon earhquake rupture trace, San Andreas Fault. *Bulletin of the Seismological Society of America*, *102*(3), 1135–1154. https://doi.org/10.1785/0120110230

Zielke, O., Klinger, Y., & Arrowsmith, J. R. (2015). Fault slip and earthquake recurrence along strike-slip faults—Contributions of high-resolution geomorphic data. *Tectonophysics*, *638*, 43–62. https://doi.org/10.1016/j.tecto.2014.11.004